



Linking titanite U–Pb dates to coupled deformation and dissolution–reprecipitation

Amy C. Moser¹ · Bradley R. Hacker¹ · George E. Gehrels² · Gareth G. E. Seward¹ · Andrew R. C. Kylander-Clark¹ · Joshua M. Garber³

Received: 1 September 2021 / Accepted: 4 March 2022
© The Author(s) 2022

Abstract

Titanite U–Pb geochronology is a promising tool to date high-temperature tectonic processes, but the extent to and mechanisms by which recrystallization resets titanite U–Pb dates are poorly understood. This study combines titanite U–Pb dates, trace elements, zoning, and microstructures to directly date deformation and fluid-driven recrystallization along the Coast shear zone (BC, Canada). Twenty titanite grains from a deformed calc-silicate gneiss yield U–Pb dates that range from ~75 to 50 Ma. Dates between ~75 and 60 Ma represent metamorphic crystallization or inherited detrital cores, whereas ~60 and 50 Ma dates reflect localized, grain-scale processes that variably recrystallized the titanite. All the analyzed titanite grains show evidence of fluid-mediated dissolution–reprecipitation, particularly at grain rims, but lack evidence of thermally mediated volume diffusion at a metamorphic temperature of > 700 °C. The younger U–Pb dates are predominantly found in bent portions of grains or fluid-recrystallized rims. These features likely formed during ductile slip and associated fluid flow along the Coast shear zone, although it is unclear whether the dates represent 10 Myr of continuous recrystallization or incomplete resetting of the titanite U–Pb system during a punctuated metamorphic event. Correlations between dates and trace-element concentrations vary, indicating that the effects of dissolution–reprecipitation decoupled U–Pb dates from trace-element concentrations in some grains. These results demonstrate that U–Pb dates from bent titanite lattices and titanite subgrains may directly date crystal-plastic deformation, suggesting that deformation microstructures enhance fluid-mediated recrystallization, and emphasize the complexity of fluid and deformation processes within and among individual grains.

Keywords Titanite · U–Pb geochronology · Deformation · Interface-coupled dissolution–reprecipitation · Coast shear zone

Introduction

Establishing the timing, duration, and rates of deformation and fluid flow in ductile shear zones is essential for understanding a host of tectonic processes such as strain partitioning, feedbacks between shallow and deep-crustal deformation, plate boundary initiation and evolution, and the

differentiation of Earth's crust. Despite their significance, directly dating ductile slip and associated fluid flow remains challenging. It is well known that deformation and fluids (re)crystallize mineral assemblages as shear zones evolve, with the resulting microstructures and compositional zoning providing direct links to the processes from which they formed (e.g., Austrheim 1987; Goncalves et al. 2012; Jamtveit et al. 2016). However, most microstructural studies of rocks deformed at high temperature have focused on minerals that are not datable using high-temperature radioactive isotope geochronology (for example, quartz and feldspar, e.g., Tullis and Yund 1987; Hirth and Tullis 1991). The microtextures of datable accessory minerals that (re)crystallize in ductile deformed rocks, therefore, provide a critical, but underexplored, window into the timing and nature of high-temperature deformation.

Of the minerals that incorporate appreciable U and Th into their crystal structures, titanite is a useful

Communicated by Daniela Rubatto.

✉ Amy C. Moser
amoser@ucsb.edu

¹ Department of Earth Science, University of California, Santa Barbara, Santa Barbara, CA, USA

² Department of Geosciences, University of Arizona, Tucson, AZ, USA

³ Department of Geosciences, The Pennsylvania State University, University Park, PA, USA

petrochronometer to directly date the record of tectonic processes preserved in metamorphic rocks. Many crustal rocks contain titanite (Frost et al. 2000), as it crystallizes in a wide range of bulk compositions and metamorphic conditions, and commonly forms crystals several hundred microns in length (Frost et al. 2000; Spencer et al. 2013; Holder et al. 2019). Titanite also incorporates many trace elements into its crystal structure that can be used to constrain ambient P – T conditions, either using direct thermometry or by connecting titanite to metamorphic assemblages (Hayden et al. 2008; Spencer et al. 2013; Garber et al. 2017; Kohn 2017). Contrary to experimental data (Cherniak 1993), data from natural rocks demonstrate that titanite remains largely unaffected by thermally mediated volume diffusion of Pb at temperatures < 750 °C (Rubatto and Hermann 2001; Kohn and Corrie 2011; Spencer et al. 2013; Stearns et al. 2016; Kohn 2017; Marsh and Smye 2017; Hartnady et al. 2019; Holder et al. 2019). Titanite may recrystallize via dissolution–reprecipitation in the presence of (typically H_2O -rich) fluids (Garber et al. 2017; Marsh and Smye 2017; Walters and Kohn 2017; Holder and Hacker 2019), undergo crystal-plastic deformation at moderate to high metamorphic temperatures (greenschist- to granulite-facies conditions), and preserve several generations of zoning and microstructures (Bonamici et al. 2015; Papapavlou et al. 2017, 2018; Gordon et al. 2021), providing a rich record of superposed metamorphic processes.

Recent advances in our understanding of titanite Pb closure temperature (Kohn and Corrie 2011; Spencer et al. 2013; Stearns et al. 2016; Garber et al. 2017; Kohn 2017; Hartnady et al. 2019; Holder et al. 2019) have cast doubt on many early interpretations of titanite U–Pb dates as cooling ages. In the absence of evidence for thermally mediated volume diffusion, titanite U–Pb dates have been variably interpreted as crystallization or recrystallization ages depending on the relationships among U–Pb dates, microtextures, and trace-element compositions. This study investigates the mechanisms of recrystallization in titanite by integrating U–Pb dates, trace-element concentrations, compositional zoning, and microstructural data from twenty titanite grains from a single calc-silicate gneiss that was metamorphosed and deformed in the Coast shear zone, British Columbia (Ingram and Hutton 1994; Klepeis et al. 1998; Rusmore et al. 2001; Andronicos et al. 2003). We demonstrate the range and complexities of processes that are responsible for titanite recrystallization at the scale of a single thin section and present a framework to link titanite U–Pb dates to the timing of deformation and metamorphic fluid flow.

Background

Effects of cooling, crystallization, fluids, and deformation on U–Pb systematics

U–Pb dates from accessory minerals may reflect one or more processes that can be tied to the tectonothermal history of a rock. Given the extensive previous work on U–Pb systematics in titanite and other U-bearing minerals, we first consider expected relationships among textural, microstructural, and elemental/isotopic observations in titanite as a function of the mechanism or process responsible for their formation (summarized in Fig. 1).

U–Pb dates are frequently interpreted as cooling ages, or the time that thermally mediated volume diffusion of Pb ceased as that mineral cooled (Fig. 1A; e.g., Dodson 1973). Experimental titanite data suggest that the Pb closure temperature for 100 μm -diameter titanite subject to a ~ 10 °C/Myr cooling rate is ~ 600 °C (Cherniak 1993). However, the length scales of Pb diffusion in natural rocks indicate a closure temperature > 750 °C, compatible with slower Pb diffusion (Kohn and Corrie 2011; Spencer et al. 2013; Stearns et al. 2016; Kohn 2017; Marsh and Smye 2017; Smye et al. 2018; Hartnady et al. 2019; Holder et al. 2019). The naturally constrained intracrystalline diffusivity of Pb in titanite is similar to the experimentally measured diffusion of Sr in titanite, which is reasonable given their similar charge and ionic radii (Cherniak 1995; LaTourrette et al. 1996). Though commonly interpreted as such without detailed, grain-scale data, titanite U–Pb dates cannot confidently be considered “Dodsonian” cooling ages unless there is evidence for volume diffusion in the spatial distribution of Pb and/or U–Pb dates. Such evidence might include variation in dates from grain core to rim, with older dates in the cores asymptotically approaching younger dates in the rims (Fig. 1A; Crank 1975) or dates that vary systematically with grain size, with larger grains yielding older dates and smaller grains yielding younger dates (Bonamici et al. 2015; Kirkland et al. 2016; Olierook et al. 2019).

Alternatively, U–Pb dates are in the simplest case interpreted as *crystallization ages*, or the time that a mineral formed below its Pb closure temperature. Growth, sector, or core–rim zoning combined with distinct U–Pb ages from compositional domains provide evidence that dates reflect the timing of crystallization (Fig. 1B–D). Variations in P , T , and/or trace-element partitioning/availability during titanite growth may produce concentric growth zoning, which broadly manifests as progressively outward-stepping compositional domains with sharp or gradational boundaries (Fig. 1B; Lucassen et al. 2011; Bonamici et al. 2015; Garber et al. 2017). In such cases, the U–Pb dates are expected to decrease from core to rim and reflect the duration of titanite

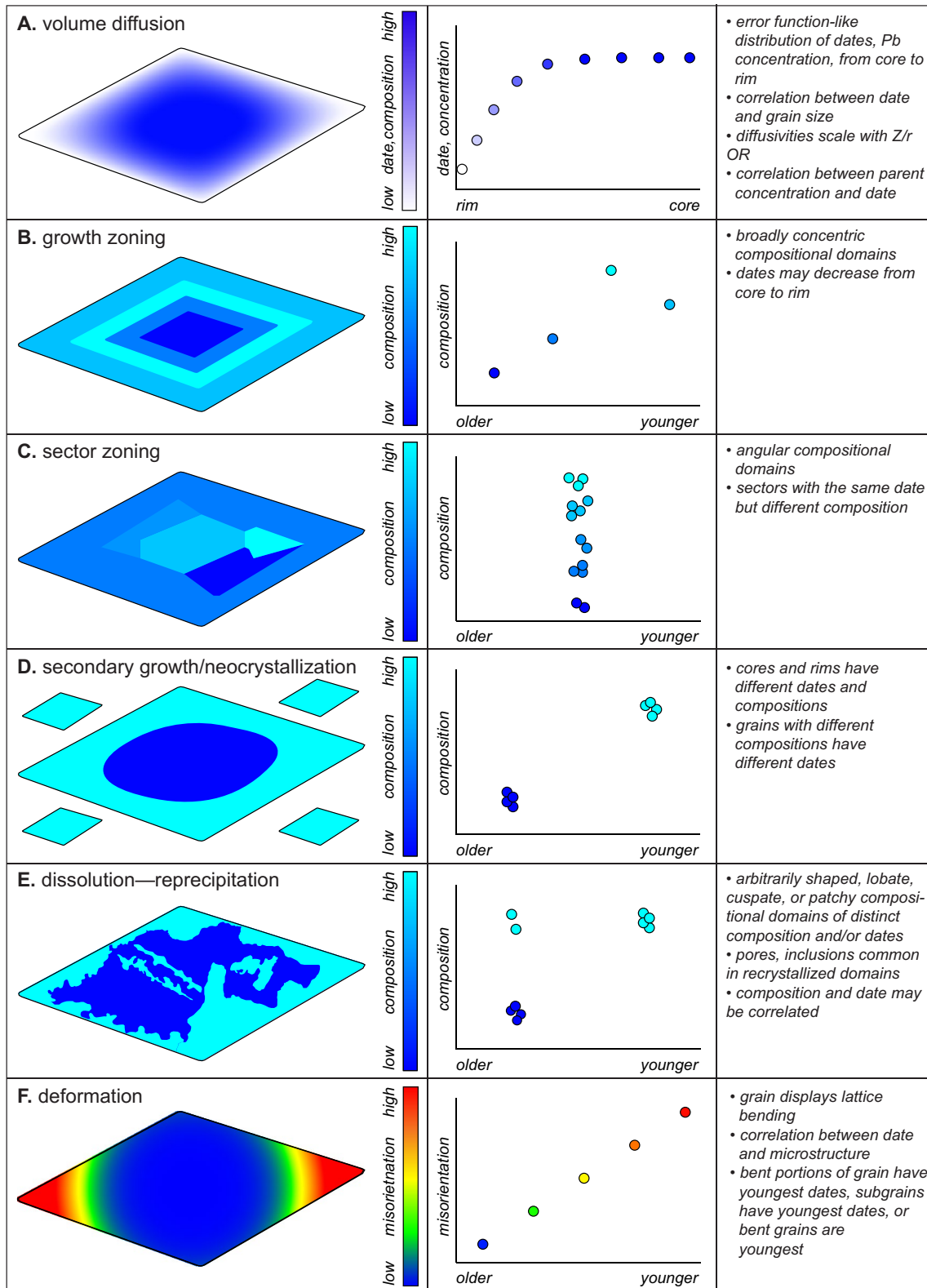


Fig. 1 Expected titanite microtextures and relationships between date and distance from the edge of the grain, composition, or intragrain misorientation for various grain-scale processes that may be recorded by titanite U–Pb dates. See main text for explanation of processes

growth. Sector zoning may also be produced during crystal growth if partition coefficients vary among different crystal faces and crystal growth outpaces intracrystalline volume diffusion (Fig. 1C; Hollister 1970; Watson and Liang 1995); in titanite, trace-element concentrations in different sectors that crystallized simultaneously may vary by a factor of three (Fig. 1C; Paterson et al. 1989; Hayden et al. 2008; Walters and Kohn 2017). Secondary titanite growth is indicated by core–rim overgrowth textures or multiple generations of compositionally distinct grains, both with clear U–Pb date populations (Fig. 1D; Bonamici et al. 2015; Garber et al. 2017; Olierook et al. 2019).

Titanite dates may also be recrystallization ages. Grains may recrystallize by interface-coupled dissolution–reprecipitation, wherein a fluid-rich interface moves through a crystal, replacing the precursor grain with the same (or similar) phase of different composition and/or date, and typically preserving the original crystal shape (Geisler et al. 2003, 2007; Putnis et al. 2005; Putnis 2009). Minerals recrystallized by dissolution–reprecipitation may preserve inward-convex, arbitrarily shaped, lobate/cusped, or patchy compositional domains that penetrate inward from the grain edges, fractures, twin planes, and/or inclusions (Fig. 1E; Geisler et al. 2003, 2007; Putnis et al. 2005; Putnis 2009). Evidence of dissolution–reprecipitation is common in monazite (Budzyń et al. 2011; Harlov et al. 2011; Williams et al. 2011; Seydoux-Guillaume et al. 2012; Hacker et al. 2015; Weinberg et al. 2020), zircon (Geisler et al. 2003; 2007; Tomaschek et al. 2003; Soman et al. 2010), and increasingly recognized in titanite (Smith et al. 2009; Spencer et al. 2013; Bonamici et al. 2015; Garber et al. 2017; Marsh and Smye 2017; Holder and Hacker 2019).

In addition to volume diffusion and (re)crystallization, the presence and movement of line defects through a crystal (i.e., dislocation creep) can redistribute trace elements (Cottrell and Bilby 1949; Turnbull and Hoffman 1954; Hoffman 1956; Hart 1957; Huang et al. 1989; Larche and Cahn 1985; Love 1964; Rabier and Puls 1989; Ruoff and Balluffi 1963; Swiatnicki et al. 1986), including radiogenic Pb (Peterman et al. 2016; Piazzolo et al. 2016; Fougereuse et al. 2021). Deformation-induced trace-element mobility in minerals has been inferred and directly observed from various microstructural, geochronology, and trace-element datasets (Reddy et al. 2006; Timms et al. 2006, 2011; MacDonald et al. 2013; Piazzolo et al. 2016; Kovaleva et al. 2017; Kirkland et al. 2018; Fougereuse et al. 2021). A number of these datasets show correlations between U–Pb date and microstructure in several dateable minerals; deformed grains, mechanical twins, and low-angle subgrain boundaries have the youngest dates and/or the greatest discordance in the U–Pb system (Moser et al. 2009; MacDonald et al. 2013; Bonamici et al. 2015; Kovaleva et al. 2017; Langone et al. 2017; Papapavlou et al. 2018; Moore et al. 2020; Fougereuse et al. 2021).

Transmission electron microscopy and atom probe investigations of geologic materials have revealed the systematic enrichment of trace elements in free dislocations and dislocation loops, and the loss or retention of trace elements along subgrain boundaries (Peterman et al. 2016; Piazzolo et al. 2016; Kirkland et al. 2018; Fougereuse et al. 2019, 2021). These data suggest that crystal-plastic deformation may partially or fully reset the U–Pb system in deformed minerals, and it is reasonable to expect that this includes titanite (Bonamici et al. 2015; Papapavlou et al. 2017, 2018; Gordon et al. 2021) even if the precise mechanisms of dislocation-facilitated Pb transport differ among minerals (e.g., Kirkland et al., 2018). U–Pb dates can be interpreted as deformation ages if a grain displays lattice misorientation (hereafter referred to as “bending” or “bent grains”), low-angle boundaries ($> 1^\circ$ but $< 10^\circ$ of misorientation across a subgrain wall), and/or dynamically recrystallized new grains ($> 10^\circ$ with respect to parent grain) and a correlation between U–Pb date and microstructure (Fig. 1F). For example, U–Pb dates may decrease with increased bending, or subgrains and/or bent grains may have the youngest dates (Fig. 1F), although examples from the literature demonstrate these relationships could be more complex if elements are redistributed within and not lost completely from the grain during dislocation creep (e.g., Kovaleva et al. 2017).

Geologic setting

The Coast Mountains Orogen is a ~1700 km-long, ~5–175 km-wide, Jurassic to Eocene calc-alkaline batholith located in westernmost British Columbia and southeasternmost Alaska (Fig. 2A; e.g., Harrison et al. 1979; Crawford and Hollister 1982; Gehrels et al. 1991). The Coast Mountains host the Coast shear zone, a 5–15 km-wide, >1200 km-long, subvertical, crustal-scale, ductile shear zone along and within the western edge of the Great Tonalite Sill (Fig. 2A; Hollister and Crawford 1986; Crawford et al. 1987; Gehrels et al. 1991; Ingram and Hutton 1994; Morozov et al. 1998; Thomas and Sinha 1999; Rasmussen et al. 2001, 2005; Andronicos et al. 2003). The dominant foliation and lineation throughout the Coast shear zone are both steep, with predominantly east-side-up kinematic indicators (e.g., Ingram and Hutton 1994). Most workers interpret these features to reflect largely dip-slip motion (e.g., McClelland et al. 1992; Klepeis et al. 1998), but some have proposed that the steep fabrics developed during transpression (Fossen and Tikoff 1998). The timing of deformation in the Coast shear zone is primarily constrained by the crystallization age of the Great Tonalite Sill, a 5–30 km-wide, sheetlike pluton that intruded synkinematically with the Coast shear zone from ~80 to 55 Ma. Deformation also affected the margins of the metamorphic country rocks to the

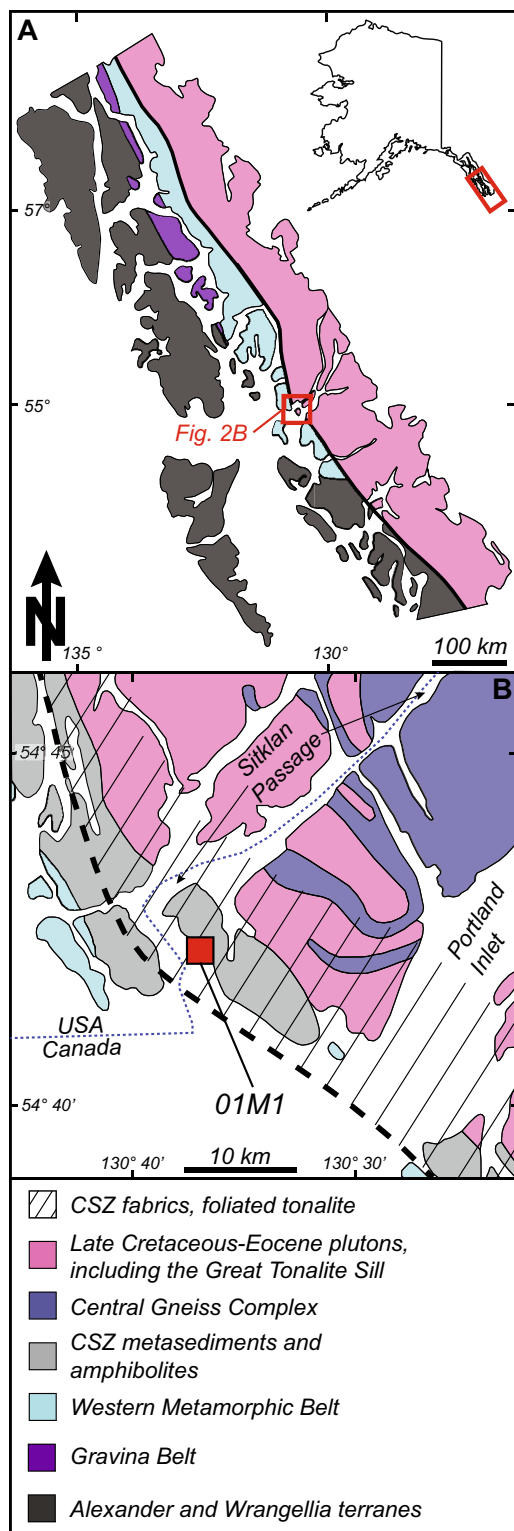


Fig. 2 **A** Location and generalized geologic map of the Coast Mountains Orogen and Coast shear zone. Thick black line delineates the main trace of the Coast shear zone. **B** Geology of Wales Island, British Columbia. Red box denotes location of the titanite-bearing calc-silicate gneiss 01M1 analyzed in this study. Thick, dashed black line marks the main trace of the Coast shear zone. After Klepeis et al. (1998)

east and west of the sill (Fig. 2; Ingram and Hutton 1994; Rusmore and Woodsworth 1994; Klepeis et al 1998).

The structural, metamorphic, and tectonic histories of these units in Sitklan Passage (location of the studied sample) have been previously studied by Klepeis et al (1998) (Fig. 2B). Cross-cutting relationships in Sitklan Passage indicate two phases of Coast shear zone deformation: an initial phase of east-side-up deformation from ~65 to 57 Ma, constrained by the crystallization age of deformed tonalites, followed by ~57–55 Ma east-side-down deformation defined by a suite of deformed pegmatites and undeformed plutons (Klepeis et al. 1998). The latter phase was concentrated in the western portion of the shear zone, hereafter referred to as the “westernmost Coast shear zone.” These data suggest ductile deformation along the Coast shear zone in Sitklan Passage ceased around 55 Ma (Klepeis et al. 1998). Early, east-side-up deformation occurred during or after decompression and heating of rocks within the shear zone, as indicated by cordierite coronas on garnet and sillimanite pseudomorphs after kyanite and staurolite in Coast shear zone metapelites (Klepeis et al. 1998). Garnet geochemistry and cordierite coronas indicate that the early deformation phase occurred at 5.6 ± 0.4 kbar and 710 ± 30 °C (Klepeis et al. 1998); there are no prior P – T estimates for the later, east-side-down deformation.

Sample description

The studied sample, 01M1, is a metasedimentary calc-silicate gneiss from Wales Island between Portland Inlet and Sitklan Passage (54.741389 N, 130.614345 W; Fig. 2B). The sampled unit comprises metamorphic country rocks intruded by Paleocene–Eocene tonalite sills and pegmatite dikes (“CSZ metasediments and amphibolites,” Klepeis et al. 1998; Fig. 2, this study) including the Great Tonalite Sill. The gneiss consists of diopside, potassium feldspar, plagioclase feldspar, Ca-amphibole, titanite, clinozoisite, biotite, quartz, calcite, white mica, chlorite, and trace zircon (Figs. 3, S1). Titanite grains are idioblastic to hypidioblastic and ~50–1000 μ m in maximum length. The bulk rock fabric consists of a foliation defined by compositional layering, with different proportions of diopside and feldspar; the long axes of most titanite grains are aligned with this fabric (Figs. 3, S1). No lineation was observed. Undulatory extinction is pervasive in feldspar, and additional deformation microstructures are limited to undulatory extinction and low-angle boundaries in a few titanite grains; other phases are mostly unaffected. No shear bands were observed in thin section. The foliation dips moderately (dip–dip direction 42/028) at the studied sample site. Projection along strike places the sample within the westernmost Coast shear zone described above. All analyses were conducted on a

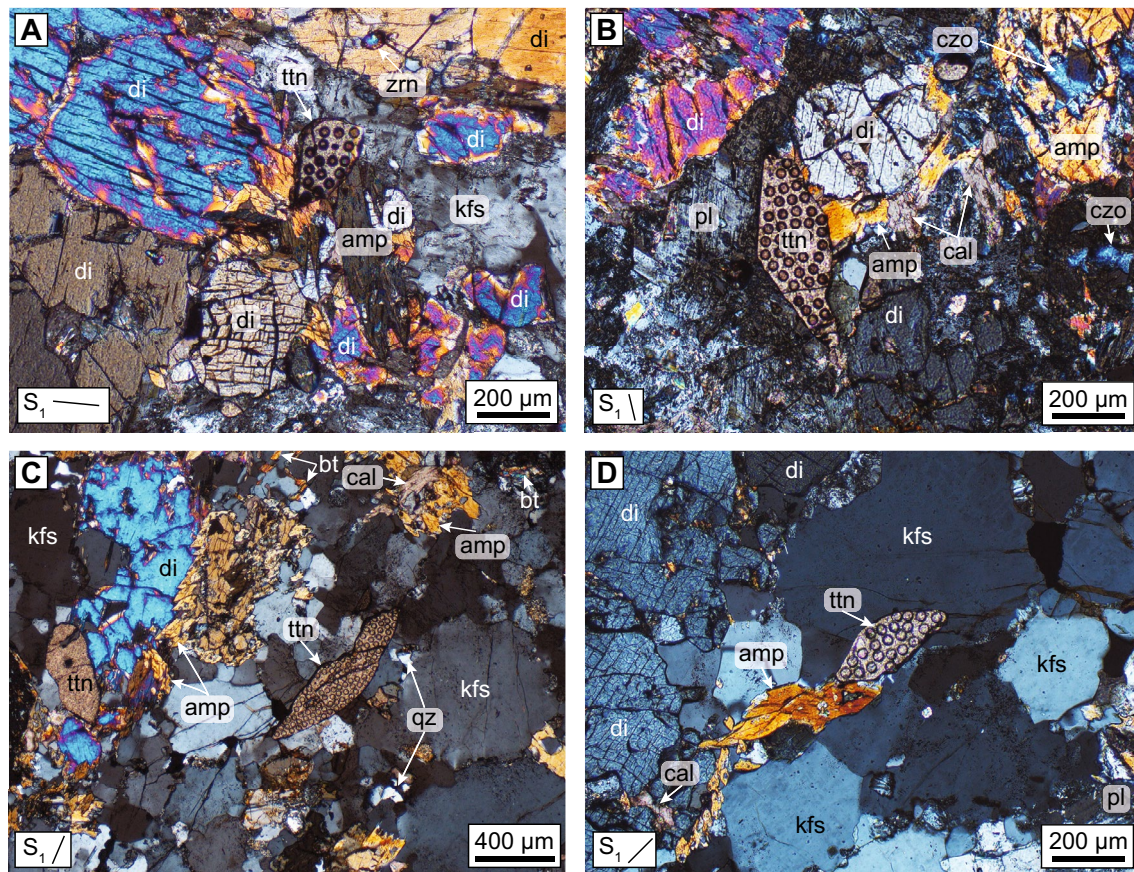


Fig. 3 Cross-polarized light images of titanite analyzed from calc-silicate gneiss 01M1. **A** Grain 4, **B** grain 12, **C** grain 19, **D** grain 20. S_1 denotes orientation of foliation (42/028, dip/dip direction) defined

by compositional layers of diopside and feldspar. *Amp* Ca-amphibole, *bt* biotite, *cal* calcite, *czo* clinozoisite, *di* diopside, *kfs* K-feldspar, *pl* plagioclase feldspar, *ttn* titanite, *qz* quartz, *zrn* zircon

single polished thin section that was cut perpendicular to the foliation.

Methods

Electron-backscatter diffraction (EBSD)

Titanite EBSD data were collected on an FEI Quanta 400F field emission source scanning electron microscope coupled with an HKL Technology Nordlys II EBSD camera at the University of California, Santa Barbara. Data were acquired at an accelerating voltage of 20 kV, a 1–5 nA beam current, a working distance of ~15 mm, and the sample surface inclined at 70° to the incident electron beam. EBSD pattern maps were acquired and indexed using Oxford/HKL Channel 5 Flamenco application. The maps were collected by electron-beam rastering, with sampling on a 2 × 2 μm grid. EBSD maps were processed with Oxford/HKL Channel 5 Tango application. Data processing included two steps:

removal of single pixels possessing a large misorientation with respect to neighboring pixels, and assignment of an average-orientation to any unindexed pixel with at least six neighboring indexed pixels of the same phase. To visualize substructure within individual grains (microstructure), maps of relative misorientation within a grain were calculated; these maps were calculated relative to a point in the approximate center of each grain.

Electron microprobe (EPMA) X-ray maps

Al, Fe, Zr, Nb, and Ce X-ray maps were collected using a 5-spectrometer Cameca SX100 EPMA at the University of California, Santa Barbara. The data were collected by moving the sample under a stationary 1–2 μm defocused beam, with a 150 or 200 ms dwell time, 20 kV accelerating voltage, and a 200 nA beam current. ProbeImage and CalcImage (Probe Software Inc.) were used to acquire and process the map data.

Laser-ablation split-stream inductively coupled plasma mass spectrometry (LASS)

U, Th, and Pb isotopes and trace elements were collected simultaneously from titanite in thin section using the LASS methodology described by Kylander-Clark et al. (2013) and Kylander-Clark (2017). A total of 1049 laser-ablation spots were analyzed on 20 titanite grains in three separate analytical sessions; all spots within individual grains were collected in the same session. U–Th–Pb isotopes were measured on a Nu Instruments Plasma 3D multi-collector ICP-MS in the first session, and on a Nu Instruments Plasma HR-ES multi-collector ICP-MS in sessions two and three. Trace elements were measured on an Agilent 7700X quadrupole ICP-MS in all sessions. These mass spectrometers were coupled to a Cetac/Photon Machines 193 nm excimer Excite laser with a HelEx cell. Titanite crystals were ablated with a 25 μm spot size and a laser fluence of $\sim 1 \text{ J/cm}^2$ at 4 Hz (sessions one and two) and 5 Hz (session three) for 60 shots per analytical spot. To remove surface contamination, two cleaning shots with 15–20 s washout were fired prior to each analysis.

Matrix-matched standard MKED1 ($1521.02 \pm 0.55 \text{ Ma}$ $^{206}\text{Pb}/^{207}\text{Pb}$ isotope dilution thermal ionization mass spectrometry date; Spandler et al. 2016) was run every ~ 8 unknowns, and was used as the primary standard for the U/Pb, Th/Pb, and Pb/Pb isotopic ratios. Titanite secondary standards BLR ($1047.4 \pm 1.4 \text{ Ma}$ concordia date, Aleinoff et al. 2007), Y1710C5 ($388.6 \pm 0.5 \text{ Ma}$ $^{207}\text{Pb}/^{206}\text{Pb}$ -corrected $^{206}\text{Pb}/^{238}\text{U}$ ID-TIMS date; Spencer et al. 2013) and Fish Canyon ($28.4 \pm 0.05 \text{ ID-TIMS}$ date; Schmitz and Bowring 2001) along with glass NIST SRM 612 (no date; Pearce et al. 1997) were interspersed in each run to monitor U–Th–Pb ratio accuracies. MKED1 was chosen as the primary standard as it is assumed to be homogeneous and have no common Pb (Spandler et al. 2016). The $^{207}\text{Pb}/^{206}\text{Pb}$ ratios of the NIST SRM 612 analyses were homogeneous and yielded single populations in-run, suggesting this assumption is valid for the dataset (Table S1E). Lower intercept, $^{207}\text{Pb}/^{206}\text{Pb}$ -corrected $^{206}\text{Pb}/^{238}\text{U}$ dates (assuming the contemporaneous Stacey and Kramers 1975 common-Pb $^{207}\text{Pb}/^{206}\text{Pb}$ values of 0.91, 0.86, and 0.83, respectively) for the secondary standards across the three analytical sessions were $1042 \pm 3 \text{ Ma}$ (BLR), $388 \pm 3 \text{ Ma}$ (Y1710C5), and $28 \pm 2 \text{ Ma}$ (Fish Canyon Tuff; Table S1), which are within 0.5, 0.0, and 0.0% of their known values, respectively, where 0.0% indicates the lower intercept dates were the same as the known reference value. The U and Pb isotopic data were reduced in IgorPro 6.37 with the Iolite 2.5 plugin using the “U–Pb Geochronology3” reduction scheme (Paton 2011). The first and last two seconds of each integration were removed prior to the downhole correction; integrations were manually trimmed to include only homogenous portions of the analyses (i.e., to remove inclusions) after the downhole correction was applied.

Two ratio uncertainties are reported for $^{207}\text{Pb}/^{235}\text{U}$, $^{206}\text{Pb}/^{238}\text{U}$, $^{207}\text{Pb}/^{206}\text{Pb}$, and $^{208}\text{Pb}/^{232}\text{Th}$ for each analysis: in-run uncertainties that should be used to compare dates from the same grain and/or the same session, and uncertainties required to compare dates across the three analytical sessions. In-run uncertainties include analytical uncertainties and an additional 2% uncertainty propagated in quadrature to each measured ratio, with additional uncertainty added (where required) to make in-run secondary standard BLR a single population within a given run (Table S1). Full dataset uncertainties ($\sim 3\%$ for $^{206}\text{Pb}/^{238}\text{U}$, $\sim 5\%$ for $^{207}\text{Pb}/^{206}\text{Pb}$) include analytical uncertainties and additional uncertainty required to make secondary standard BLR ratios a single population across the entire dataset. The $^{207}\text{Pb}/^{235}\text{U}$ uncertainties were recalculated using the propagated uncertainties in $^{206}\text{Pb}/^{238}\text{U}$ and $^{207}\text{Pb}/^{206}\text{Pb}$, as ^{235}U was not measured but calculated assuming a $^{238}\text{U}/^{235}\text{U}$ of 137.88. The analytical precision afforded by the laser-ablation approach is such that using the updated $^{238}\text{U}/^{235}\text{U}$ value does not change our results. The titanite U–Pb dates were calculated assuming a Stacey and Kramers (1975) common-Pb $^{207}\text{Pb}/^{206}\text{Pb}$ ratio of 0.83 ± 0.04 , which matches the upper Tera-Wasserburg concordia intercept defined by the distribution of U–Pb ratios in the analyzed titanite (Fig. 4). As with the individual U–Th–Pb ratios, in-run and whole dataset uncertainties are also reported for the $^{207}\text{Pb}/^{206}\text{Pb}$ -corrected ^{206}Pb – ^{238}U dates. NIST SRM 612 was used as the primary standard for the trace elements (Pearce et al. 1997). The trace-element data were reduced using IgorPro 6.37 with the Iolite 2.5 plugin using the “Trace Elements” data reduction scheme, and assuming 19.2 wt % Ca in the unknown titanite analyses. The trace-element concentrations for secondary trace-element standard MKED1 were within $\sim 10\%$ of the expected values for the reference material, which is typical for use of NIST glasses as a primary reference material for trace elements (Liu et al. 2008).

U and Pb concentration calculations

Reported titanite U concentrations from the Nu Instruments Plasma 3D multi-collector and Nu Instruments Plasma HR-ES multi-collector ICPs were calculated in Iolite using MKED1 (Spandler et al. 2016) as a primary standard. NIST SRM 612 U concentrations were homogeneous within error within each session, although they are inaccurate by up to $\sim 15\%$ (Table S1). Therefore, even if the reported U concentrations of unknown titanites are inaccurate, the homogeneity of the NIST SRM 612 values suggests that measured U concentrations systematically deviate from their true values by the same amount and are therefore comparable within the same session. Reported U concentration uncertainties include additional uncertainty added in quadrature to make

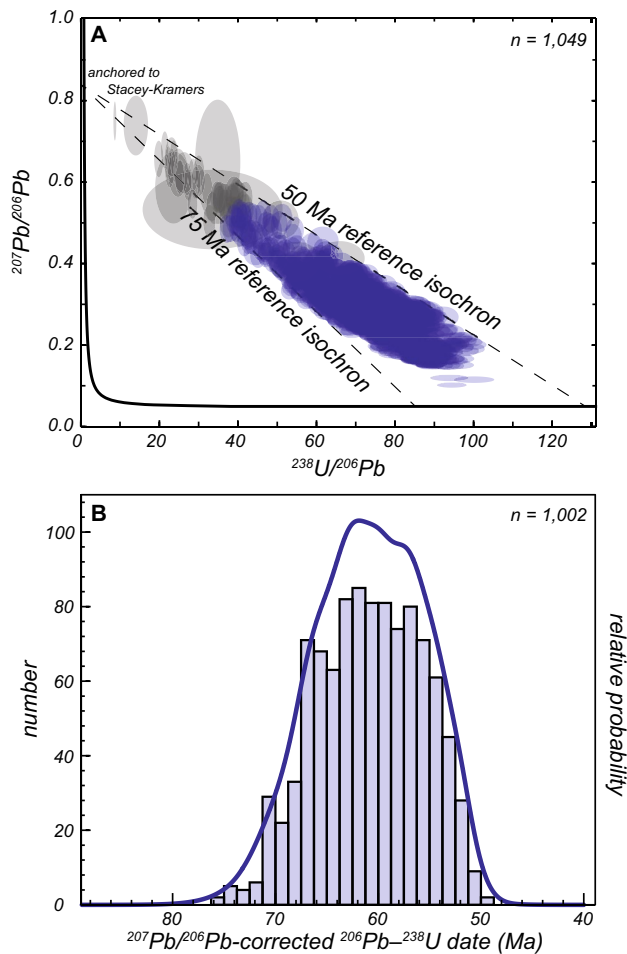


Fig. 4 **A** Tera-Wasserburg concordia diagram of all 1049 titanite laser-ablation analyses from this study. Uncertainties plotted are those required to make secondary standard BLR a single population across all three analytical sessions. Gray ellipses indicate analyses with in-run U–Pb date uncertainties > 10% that were removed from the final dataset. Blue ellipses indicate analyses with in-run U–Pb date uncertainties < 10%. Isochrons anchored to Stacey and Kramers (1975) common Pb ratios for the oldest (75 Ma) and youngest (50 Ma) date are shown for reference. **B** Histogram and probability density function of 1002 U–Pb dates with uncertainties < 10% used in the final dataset

secondary standard NIST SRM 612 a single population in-run (Table S1).

^{206}Pb , ^{207}Pb , and ^{208}Pb concentrations were calculated from U concentrations, using the downhole-corrected $^{206}\text{Pb}/^{238}\text{U}$, $^{207}\text{Pb}/^{206}\text{Pb}$, and $^{208}\text{Pb}/^{206}\text{Pb}$ ratios (with MKED1 as the primary standard) and molar masses of ^{238}U and the respective Pb isotopes (see also Garber et al. 2020a). ^{204}Pb was calculated from raw $^{204}\text{Pb}/^{206}\text{Pb}$ of the unknowns scaled by a factor required to make NIST SRM 612 $^{204}\text{Pb}/^{206}\text{Pb}$ ratios the known value for each run. We calculated Pb concentrations in this manner rather than using the values produced in iolite as iolite assumes the isotopic ratios in the reference

material and the unknowns are the same (Paton 2011). Iolite's approach, therefore, returns incorrect Pb concentrations for minerals with significant radiogenic Pb. The total Pb concentrations for secondary standards BLR (Aleinkoff et al. 2007) and NIST SRM 612 calculated in this manner overlap previously reported values (Table S1). Like the uncertainties in $^{206}\text{Pb}/^{238}\text{U}$ and $^{207}\text{Pb}/^{206}\text{Pb}$ discussed above, 2% uncertainty was added in quadrature to the $^{208}\text{Pb}/^{206}\text{Pb}$ and $^{204}\text{Pb}/^{206}\text{Pb}$ ratios; additional uncertainty was added where required to make secondary standards BLR ($^{208}\text{Pb}/^{206}\text{Pb}$) and NIST SRM 612 ($^{204}\text{Pb}/^{206}\text{Pb}$) a single population in-run. Only in-run uncertainties are reported for the $^{208}\text{Pb}/^{206}\text{Pb}$ and $^{204}\text{Pb}/^{206}\text{Pb}$ ratios as Pb concentrations were only compared within individual sessions. Uncertainties in the concentrations of the Pb isotopes were propagated in quadrature based on the U concentration uncertainties and uncertainties in the U/Pb and/or Pb/Pb ratios used in each individual Pb isotope concentration calculation. The total Pb concentration uncertainty includes the uncertainties of ^{204}Pb , ^{206}Pb , ^{207}Pb , and ^{208}Pb added in quadrature. The fraction of common ^{206}Pb and ^{207}Pb in each analysis was calculated from the measured $^{207}\text{Pb}/^{206}\text{Pb}$, radiogenic $^{207}\text{Pb}/^{206}\text{Pb}$ for the $^{207}\text{Pb}/^{206}\text{Pb}$ -corrected $^{206}\text{Pb}-^{238}\text{U}$ date and assumed Stacey-Kramers (1975) $^{207}\text{Pb}/^{206}\text{Pb}$ value (0.83) following the approach outlined by Williams (1998). The fraction of common ^{208}Pb was similarly calculated from the fraction of common ^{206}Pb , Stacey-Kramers (1975) $^{208}\text{Pb}/^{206}\text{Pb}$ value (2.07) for the $^{207}\text{Pb}/^{206}\text{Pb}$ -corrected $^{206}\text{Pb}-^{238}\text{U}$ date, and measured $^{208}\text{Pb}/^{206}\text{Pb}$ (Williams 1998; Garber et al. 2020b). This approach circumvents assumptions about data concordance and the precision and accuracy of using a ^{204}Pb correction. The equations used in the Pb concentration and common Pb fraction calculations can be found in the supplemental material.

Erf⁻¹ calculations

A normalized concentration gradient that results from volume diffusion is defined by Crank (1975):

$$\left(\frac{C - C_r}{C_c - C_r} \right) = \text{erf} \left(\frac{x}{\sqrt{4Dt}} \right),$$

where C is the concentration at a given spot, C_r is the concentration at the rim, C_c is the concentration at the core, x is the distance from the edge of the grain, and D is the diffusivity for a given duration of time (t). For the purposes of treating the concentration data in each grain as a diffusion experiment, we define C_r and C_c as the minimum and maximum concentration within each grain, regardless of whether they occur at the rim or core. Rearranging this equation, the inverse error function of the normalized data that results from volume diffusion is a line:

$$\operatorname{erf}^{-1}\left(\frac{C - C_r}{C_c - C_r}\right) = \frac{x}{\sqrt{4Dt}}$$

with slope

$$m = \frac{1}{\sqrt{4Dt}}.$$

Therefore, for single-element data, this approach can be used to calculate the diffusivity of that element if the duration of time at constant temperature is known.

The role of volume diffusion at the grain scale in the analyzed titanite grains was assessed by calculating the inverse error function of the normalized Pb and trace-element concentrations. The linearity of the normalized erf^{-1} as a function of distance from the grain edge was evaluated by calculating the correlation coefficient (Pearson's r) and the r^2 values of linear regressions through these data. The relative uncertainties assigned to the erf^{-1} values were equivalent to the relative uncertainties of the in-run propagated (dates) and raw analytical (trace-element) uncertainties.

Zr-in-titanite thermobarometry

Zr-in-titanite temperatures were calculated using the calibration of Hayden et al. (2008). A pressure of 5.6 ± 0.4 kbar was assumed based on thermobarometry of a metapelite exposed near the studied sample (Klepeis et al. 1998). The presence of quartz in the studied sample indicates that $a_{\text{SiO}_2} = 1$. Because rutile is absent, the a_{TiO_2} was assumed to be 0.75 ± 0.25 , as a_{TiO_2} in titanite-bearing rocks is likely ≥ 0.5 (Chambers and Kohn 2012; Ghent and Stout 1984; Kapp et al. 2009). Two Zr-in-titanite temperature uncertainties are quoted herein: the first incorporates the analytical uncertainties on the Zr concentrations and the cited uncertainties on the assumed pressure and a_{TiO_2} , whereas the other excludes uncertainties related to pressure and a_{TiO_2} (which implicitly assumes pressure and a_{TiO_2} were constant during titanite (re) crystallization).

Results

A summary of $^{207}\text{Pb}/^{206}\text{Pb}$ -corrected ^{206}Pb - ^{238}U dates (hereafter simply referred to as "U–Pb dates"), Zr-in-titanite temperatures, microstructures, zoning, and trace-element-date patterns for each of the analyzed grains is reported in Table 1. The complete U–Pb isotopic data, erf^{-1} calculations, Zr-in-titanite temperatures, trace-element data, EBSD texture component maps, and EPMA X-ray maps are contained in the supplemental material.

U–Pb dates

U–Pb dates from 1,049 spot analyses across 20 titanite grains from sample 01M1 range from ~ 75 to 50 Ma (Fig. 4). Some individual titanite grains preserve almost this entire range in dates (e.g., grains 3, 16; Table 1); other grains yielded a smaller range, sampling various subsets of the thin section-scale date distribution (e.g., grains 4, 13, 17; Table 1). We excluded 47 spots with uncertainties greater than 10% from the erf^{-1} calculations and date, trace-element, and microstructural comparisons, as the large errors preclude meaningful interpretations from these spots (Fig. 4).

Erf^{-1} calculations

Figure 5 presents erf^{-1} plots of normalized Pb, Sr, Al, and Ce concentration for grains 3, 7 and 20, as these grains reflect the array of grain sizes observed in the sample. Al (high diffusivity), Sr and Pb (intermediate diffusivity), Ce (low diffusivity) are used to represent the spectrum of elemental diffusivity rates in titanite (Cherniak 1993, 1995; LaTourrette et al. 1996; Holder et al. 2019). Sr may also be considered a proxy for Pb diffusion, as the two elements have identical charge and similar ionic radii (LaTourrette et al. 1996; Holder et al. 2019). In general, the correlation coefficients and r^2 values of the linear regressions of the erf^{-1} calculations (including Pb) for each grain are small, and many of the r^2 values themselves are negative (Figs. 5, S2). This observation still holds when radiogenic and common Pb are considered separately (Fig. S2). Negative correlation coefficients in these plots are a function of the way we have defined C_r and C_c as the minimum and maximum concentrations of the grain rather than the defined rim and core, and thus demonstrate instances where concentrations increase rather than decrease at the grain edges. Negative r^2 values indicate modeled linear regressions that are a poorer fit to the data than a horizontal line. Even those data with high correlation coefficients do not define a line (e.g., total Pb in grain 15, Fig. S2O), which points to the effect of outliers on Pearson's r values. Although these observations indicate that Pearson's r is an imperfect measure of correlation for this reason, it still shows that the erf^{-1} plots reveal no correlation between concentration and spot location within a grain. Correlation coefficients for U concentrations vs. U–Pb date (to assess the role of Pb diffusion driven by U concentration gradients; Paul et al. 2019) range from -0.5 to $+0.7$, but most values cluster around zero (Figs. 5 M–O, S3).

Table 1 Summary of titanite U–Pb dates, zoning, microstructures, and trace-element signatures

Grain	Grain length (μm)	Dates (Ma) ^a	Zr-in-ttn (°C) ^b	Date and Zr correlated? ^c	Misorientation (°) ^d	LABs ^e	Zoning ^f	Date-trace-element patterns	Interpretation ^g
1	300	68–57	720–762	N	2	N	p	None	Diss–repr
2	275	66–53	689–741	N	8	Y	l–c, p	Youngest dates highest REE concentrations	Def ± diss–repr
3	700	76–55	706–754	N	4	Y	l–c, p	None	Def ± diss–repr
4	250	60–51	704–749	N	12	Y	l–c	None	Def ± diss–repr
5	375	75–58	685–763	Y	1	N	l–c	Youngest dates highest REE, Zr concentrations	Diss–repr
6	550	67–56	704–773	N	3	N	l–c	None	Diss–repr
7	525	69–52	702–785	N	80	Y	c–r, l–c	REEs, Zr bimodal, not correlated with date	Def ± diss–repr
8	425	72–54	709–756	Y	2	N	l–c, p	REEs, Y, Zr, Hf concentrations increase with younging date	Diss–repr
9	500	67–50	713–770	Y	2	N	l–c	REEs, Y, Zr, Hf, Fe concentrations increase with younging date Sr decreases with younging date	Diss–repr
10	500	69–51	709–769	N	1	N	l–c	REEs, Y increase with younging date	Diss–repr
11	350	77–59	712–775	Y	1	N	l–c	LREEs, Zr, Nb, Hf increase with younging date	Diss–repr
12	500	70–53	721–776	Y	1	N	c–r, l–c	REEs, Y, Zr, Hf, Fe concentrations increase with younging date	Diss–repr
13	375	59–51	749–780	N	8	Y	l–c	None	Def ± diss–repr
14	250	68–55	706–779	Y	1	N	c–r, p	REEs, Y, Zr, Hf increase with younging date	Diss–repr
15	275	65–52	747–779	N	2	N	l–c	REEs, Y increase with younging date Youngest dates lowest Al concentrations	Diss–repr
16	400	71–53	709–771	Y	2	N	c–r, l–c, p	REEs, Y, Zr, Hf concentrations increase with younging date Sr, Nb, Ta decrease with younging date	Diss–repr
17	550	59–54	765–783	N	8	Y	l–c	None	Def ± diss–repr
18	1050	68–50	703–743	N	5	N	p	LREEs bimodal, not correlated with date; MREEs, HREEs, Y, Al Fe, Sr, Nb, Ta decrease with younging date	Def ± diss–repr
19	900	69–50	714–740	Y	2	N	l–c, p	LREEs, Zr, Hf increase with younging date Al, Nb, Ta decrease with younging date	Diss–repr
20	325	67–51	701–743	Y	2	N	l–c, p	Zr, Hf increase with younging date Al decreases with younging date	Diss–repr

^a²⁰⁷Pb/²⁰⁶Pb-corrected ²⁰⁶Pb–²³⁸U date using Stacey–Kramers common Pb value of 0.83

^bCalculated using Hayden et al. (2008) Zr-in-ttn calibration, P = 5.6 kbar, $a_{\text{SiO}_2} = 1$, $a_{\text{TiO}_2} = 0.75$

^cY: Zr-in-titanite temperature and date are correlated; N: Zr-in-titanite temperature and date are not correlated

^dMaximum intragrain misorientation relative to point in center of grain

^eMisorientation across low-angle grain boundaries (LABs) is < 10°

^fc–r core–rim, l–c lobate–cuspat, p patchy (see main text for explanation)

^gdiss–repr dissolution–reprecipitation, def deformation

Sample-scale Zr-in-titanite temperatures and trace-element concentrations

Calculated Zr-in-titanite temperatures range from ~700 to 780 °C (Fig. 6A, Table 1). The calculated Zr-in-titanite temperatures from the oldest U–Pb spots overlap published equilibrium thermometry constraints from a nearby Coast shear zone metapelite (~700 °C; Klepeis et al. 1998), suggesting that the Zr-in-titanite temperatures are broadly accurate. U–Pb date and Zr-in-titanite temperature are not correlated at the sample scale (Fig. 6A). It is notable, however, that most Zr-in-titanite temperatures > 750 °C are from spots younger than ~65 Ma. With the exception of La_N/Sm_N , which increases with decreasing date, there are no consistent sample-scale trends in date vs. trace-element content (Fig. 6B–D).

Zoning and individual grain trace-element concentrations

EPMA X-ray maps reveal three types of zoning in the analyzed titanite crystals; the zoning is most evident in the Al and Ce maps (Figs. 7, 8, 9). Seventeen grains have inward-penetrating, lobate–cusped rims (Figs. 7A, 8A) that are particularly distinctive in the Al maps (Fig. 8A), but also mimicked by the Ce zoning in ten of these grains (e.g., Fig. 7A). Seven titanite grains display Al, Ce, and Nb zoning that is patchy or irregular (Fig. 8A). No porosity or inclusions are associated with the lobate–cusped rims or areas of patchy zoning, as revealed by BSE imaging (Fig. S4). Four grains exhibit core–rim zoning in the Ce X-ray maps, with low-Ce cores and high-Ce rims, but these same grains have lobate–cusped rims or patchy zoning in the Al maps (Figs. 9A, S5N, S5P).

Correlations among date and some measured trace elements exist in 14 of the grains, but the trace-element–date correlations vary randomly from grain to grain (Figs. 7, 8, 9). For example, young spots in some grains have higher concentrations of nearly every measured trace element (e.g., grain 12; Fig. 9B and C). Other grains have more-complex date–trace-element correlations, with some trace-element concentrations increasing with younging date and others decreasing (e.g., grain 19; Fig. 8B and C), only a few elements correlated with date (grain 20, Fig. 7B and C), or a bimodal distribution of trace-element concentrations that are not correlated with date (e.g., grain 7; Fig. S5G). Six of the analyzed grains yielded no relationships among date and any measured trace element (e.g., grain 3, Fig. S5C).

Intracrystalline deformation

The degree of intracrystalline deformation is variable among the grains. Thirteen of the analyzed titanite have < 3° of

misorientation with respect to the center of the grain; these titanite crystals also lack low-angle grain boundaries (1–10° of misorientation; e.g., Figs. 7A, 8A, 9A, Table 1). Six of the remaining titanite grains show ~4–12° of lattice bending, with one grain having up to 80° of misorientation relative to the central reference point (Fig. 10A–D). Six of the seven bent grains also have low-angle boundaries (Fig. 10, Table 1). The bent grains are not oriented differently with respect to the bulk rock fabric compared to the unbent crystals and are not in microstructurally different portions of the rock (e.g., in shear bands) (Fig. S1). This suggests there is no systematic control on whether the titanite lattices were bent during deformation. Most low-angle boundaries and bent portions of grains are found at grain tips (Fig. 10). Of the seven grains with subgrains, low-angle grain boundaries, and/or significant lattice bending, four display relationships between date and lattice bending (grains 2, 3, 7, 18; Fig. 10A–D) and three have no dates older than ~60 Ma (grains 4, 13, 17; Fig. 10E–G).

Discussion

Volume diffusion of Pb and other trace elements

The erf^{-1} calculations suggest that the ~25 Myr spread in titanite U–Pb dates does not reflect a diffusive Pb-loss process at the scale of individual grains (Figs. 5, S2). The erf^{-1} of the normalized Pb concentration and distance from the edge of a grain are not correlated in any of the titanite grains (Figs. 5A–C, S2). The exception is grain 15, which has a correlation coefficient for Pb vs. distance of ~0.76 (Fig. S2O). However, in this grain, distance and Sr concentration are negatively correlated, whereas the opposite relationship is expected from volume diffusion (Fig. S2O). If Pb and Sr behave similarly with respect to intracrystalline diffusion in titanite (LaTourrette et al. 1996; Marsh and Smye 2017), the contrasting Pb vs. Sr observations make it unlikely that Pb moved via volume diffusion in this grain. Further, none of the measured trace elements yield error function-like correlations between concentration and distance from the grain edge in any of the crystals (Figs. 5, S2). No element, Pb included, appears to have moved via volume diffusion at the grain scale; this requires that the titanite U–Pb dates are not cooling ages, even though the calculated Zr-in-titanite temperatures approached conditions at which Pb diffusion in titanite has been observed in other rocks (e.g., Garber et al. 2017). We note that our approach precludes assessment of volume diffusion at lengthscales smaller than the analytical spot size (25 μm).

We tested for the effects of U zoning on volume diffusion of Pb by evaluating the relationship between date and U concentration in each titanite grain (Paul et al. 2019). It has been

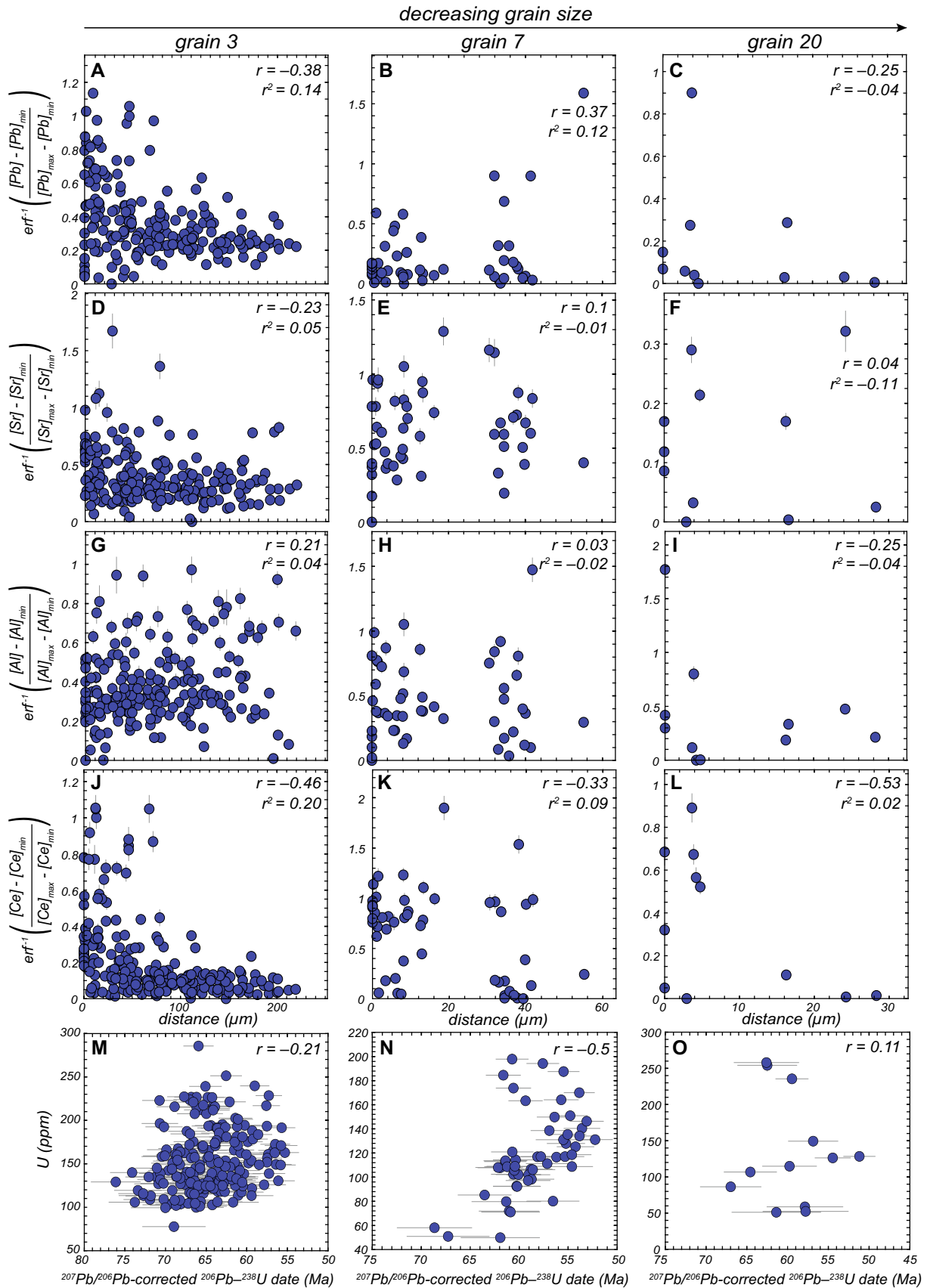


Fig. 5 Representative Pb (A–C), Sr (D–F), Al (G–I), and Ce (J–K) erf^{-1} calculations from grains 3, 7, and 20. Distance measurements are the minimum distance of the spot from the nearest grain edge. Each distance measurement has an associated $\pm 25 \mu\text{m}$ uncertainty not shown to preserve clarity. The correlation coefficients (r) and r^2 values of linear regressions between distance from the grain edge and the erf^{-1} of normalized concentration are low or negative, indicating that the spatial distribution of elements do not define an error function at the grain scale and are unlikely to have formed by thermally mediated volume diffusion. (M–O) Date and U concentrations are not strongly negatively correlated at the individual grain scale, indicating that heterogeneous parent concentrations did not drive Pb volume diffusion

shown elsewhere that heterogeneous U distributions result in Pb concentration gradients that can drive volume diffusion, producing negative correlations between U–Pb date and U concentration (Paul et al. 2019). Except for three grains (grains 5, 7, and 13), U–Pb date and U are not negatively correlated in the Coast shear zone titanites (Figs. 5M–O, S2), suggesting that U zonation did not obfuscate straightforward core–rim variations in U–Pb date. Rather than volume diffusion, the relationship between date and U concentration in three grains more likely reflects changing fluid composition during interface-coupled dissolution–reprecipitation (see “Dissolution–reprecipitation”).

Dates vs. Zr-in-ttn temperature, trace-element compositions

With the exception of La_N/Sm_N , there is no clear correlation between the titanite U–Pb dates and trace-element compositions or Zr-in-titanite temperature at the scale of the entire dataset (Fig. 6). This implies that the titanite did not simultaneously undergo the same (re)crystallization process, or such a process was variably recorded by individual grains. It is also worth noting that Zr-in-titanite temperatures $> 750 \text{ }^\circ\text{C}$ are restricted to dates younger than 65 Ma, and that Zr-in-titanite temperatures younger than 65 Ma are bimodal (~ 725 or $\sim 770 \text{ }^\circ\text{C}$). Although these temperatures cannot be resolved if the uncertainties on pressure, a_{TiO_2} , and Zr concentration are all considered, the underlying bimodality in Zr concentrations can be differentiated outside of their analytical uncertainties (Fig. 6A). As such, the sample effectively records two distinct Zr concentrations within and between different titanite grains that (re)crystallized at the same time. Such bimodality is typically ascribed to sector zoning in titanite (Paterson et al. 1989; Hayden et al. 2008; Walters and Kohn 2017), yet none of the grains are obviously sector zoned (Fig. S5).

A closer look at the Zr-in-titanite data reveals multiple date vs. temperature patterns (Fig. 11) across individual grains. Date and temperature are correlated in nine grains; in these grains, temperature increases with younging date (Fig. 11A). We suggest the $\sim 700 \text{ }^\circ\text{C}$ temperatures from spots

yielding the oldest dates (~ 75 – 60 Ma) reflect the ambient temperature during initial crystallization, as the temperatures overlap prior constraints for the beginning of Coast shear zone deformation (Klepeis et al. 1998). It is expected that the ambient metamorphic temperature increased during intrusion of the Great Tonalite Sill at ~ 65 Ma; the higher temperatures from the younger (~ 60 – 50 Ma) spots likely record peak metamorphic conditions at this time. The correlation between date and temperature in these grains represent instances of dates and Zr contents reset at the same time, most likely by the same process.

The data patterns from the remaining grains are responsible for the bimodality of temperature data at the sample scale. Three grains yield the full sample range in dates, but the Zr-in titanite temperatures are consistently low (~ 700 – $730 \text{ }^\circ\text{C}$; Fig. 11B). An additional subset of grains yields a more restricted range of young dates (≤ 65 Ma) and the calculated temperatures are largely $> 750 \text{ }^\circ\text{C}$ (Fig. 11C). Two grains produce among the youngest dates in the dataset (< 60 Ma) with all temperatures $> 750 \text{ }^\circ\text{C}$ (Fig. 11D). A single titanite crystal likewise exhibits only young dates (< 60 Ma), but with $< 750 \text{ }^\circ\text{C}$ temperatures (Fig. 11E). Finally, U–Pb dates and Zr contents of the three remaining grains are uncorrelated and encompass the entire date and temperature range of the dataset (Fig. 11F). These data demonstrate that U–Pb and Zr resetting was highly variable at the scale of individual grains.

There are no consistencies among the microstructures, compositional zoning, or grain size within the above groupings of titanites (Table 1; Fig. S5), nor are they spatially related within the thin section (Fig. S6). These data imply that localized, grain-scale processes heterogeneously recrystallized the titanite at the scale of a single thin section and within single crystals, leading to the absence of clear sample-scale (or in some cases, even grain-scale) trends. In the following section, we explore these recrystallization processes as revealed by the relationships among dates, zoning, trace-element compositions, Zr-in-titanite temperatures, and microstructures.

Localized, grain-scale processes recorded by titanite U–Pb dates

Dissolution–reprecipitation

The zoning textures and the relationships between dates and trace-element concentrations suggest fluid-driven recrystallization affected all the titanite grains analyzed in this study. For example, fluid-driven recrystallization textures are ubiquitous in the chemical zoning of the analyzed titanite (Figs. 7, 8, S5). Each of the twenty analyzed titanites preserves either lobate–cusped rims and/or patchy zoning in at least one element (Figs. 7A, 8A, 9A, S5), although

Fig. 6 All $^{207}\text{Pb}/^{206}\text{Pb}$ -corrected ^{206}Pb – ^{238}U dates vs. **A** Zr-in-titanite temperature (T , °C), **B** $\text{La}_\text{N}/\text{Sm}_\text{N}$, **C** $\text{Gd}_\text{N}/\text{Yb}_\text{N}$, and **D** $\text{Sm}_\text{N}/\text{Eu}_\text{N}$. $\text{Sm}_\text{N}/\text{Eu}_\text{N}$ is plotted as an alternative to Eu/Eu^* as Eu concentrations are relatively constant across the dataset and serve as an additional means to normalize the trace-element data. Date uncertainties are those required to make secondary standard BLR a single population across all three analytical sessions. Two representative Zr-in-titanite temperature uncertainties are shown: one for Zr concentration uncertainties only, and another that includes uncertainties in pressure and a_{TiO_2} . REEs are normalized to chondritic meteorite values of McDonough and Sun (1995). Normalized trace-element ratio uncertainties are 2σ analytical uncertainties propagated in quadrature

several grains have comparatively simple core–rim Ce zoning (e.g., Fig. 9A). The inward-penetrating, lobate–cusate rims are diagnostic of interface-coupled dissolution–reprecipitation recrystallization, in which a fluid-driven reaction boundary propagates into the crystal along grain rims, cracks, twin planes, or around inclusions (Geissler et al. 2003, 2007; Holder and Hacker 2019; Putnis et al. 2005; Putnis 2009; Fig. 1E). However, even the titanite grains that lack these features may have been affected by fluids. Intra-grain interfaces become lobate–cusate when the migrating interface becomes pinned by impurities such as inclusions (e.g., Ruiz-Agudo and Putnis 2012); without these impurities, the reaction boundary may be near-planar and produce more geometrically straightforward core–rim relationships. Given that the grains with simple core–rim Ce zoning also have lobate–cusate or patchy domains in the Al maps (Fig. S5G, L, N, P), we suggest that all the titanite rims record the propagation of dissolution–reprecipitation reactions.

In addition to the chemical zoning textures, the absence of systematic, reproducible variations (Fig. 6) among the dates and trace-element compositions can also be explained by the effects of dissolution–reprecipitation. The precise trace elements that correlate positively or negatively with date differ from grain to grain (Table 1; Figs. 8B and C, 9B and C), and some grains yield few or no clear relationships with any trace elements (Figs. 7B and C, Table 1). For example, dates are roughly correlated with all the REEs in ten of the titanite crystals, with Zr content in nine grains, and with Al content in three grains (Table 1; Figs. 7B and C, 8B and C, 9B and C). During dissolution–reprecipitation, the fluid composition at the reaction front continually evolves as the precursor grain dissolves and reprecipitates, potentially resulting in evolving fluid compositions at the individual grain scale (Lippmann 1980; Putnis and Mezger 2004; Putnis et al. 2005; Putnis 2009). If the local fluid composition controls the composition of the reprecipitated phase(s), and if the local fluid composition evolves as each titanite dissolution–reprecipitation reaction proceeds, the extent to which U–Pb dates and trace-element contents are reset may differ within and among individual grains (Fig. 1E; Geisler 2007; Hacker et al. 2015; Holder and Hacker 2019; Putnis and Mezger 2004; Putnis et al. 2005; Putnis 2009). Alternatively,

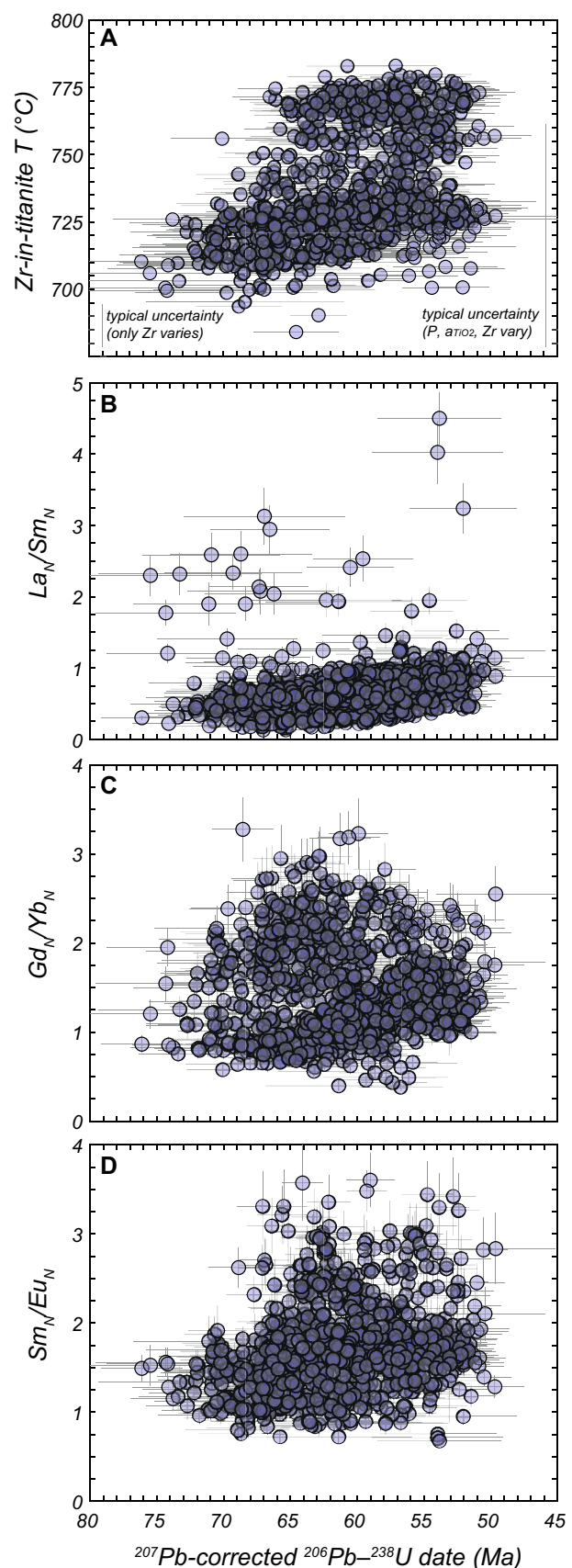
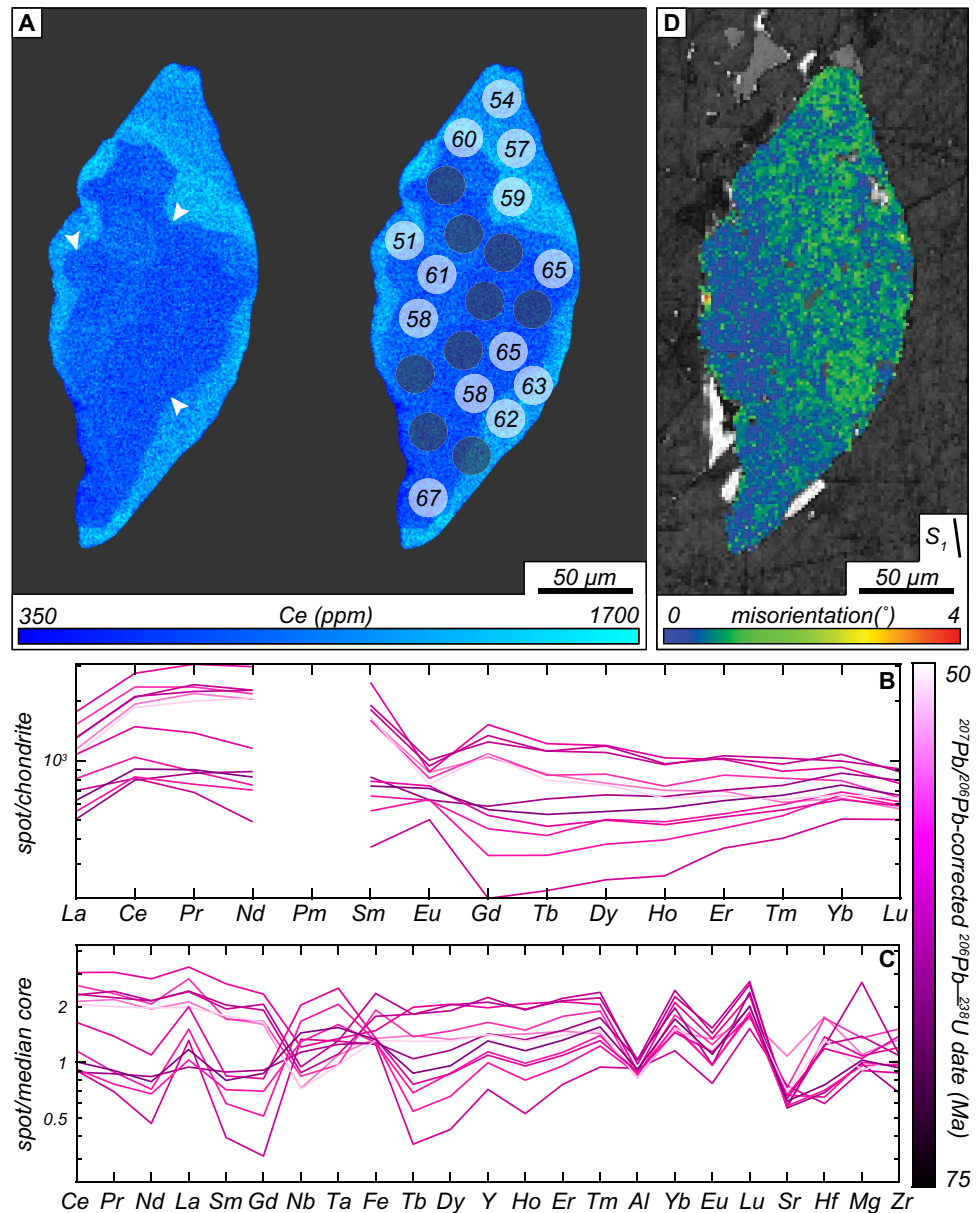


Fig. 7 Undeformed titanite grain (grain 20) displaying lobate–cusped zoning, one of three zoning patterns observed in the dataset. **A** Ce X-ray map, **B** chondrite-normalized REEs, **C** spider diagram of all measured trace elements normalized to the median dataset core values, and **D** misorientation map. Maximum and minimum concentrations in **A** were quantified using LASS data. Translucent white spots in **A** indicate the location of LASS analyses and the associated U–Pb dates (Ma). In-run date uncertainties from the dark gray spots are > 10% and were removed from the final dataset. In-run, 2σ uncertainties on U–Pb dates for this grain are 2–5 Ma. White arrows in **A** denote lobate–cusped rim, which is compatible with dissolution–reprecipitation. The elements in this and the other spider diagrams are arranged in compatibility order in titanite (Shannon 1976). Zr and Hf concentrations increase with younging date in this grain, whereas Al concentrations decrease with younging date (C)

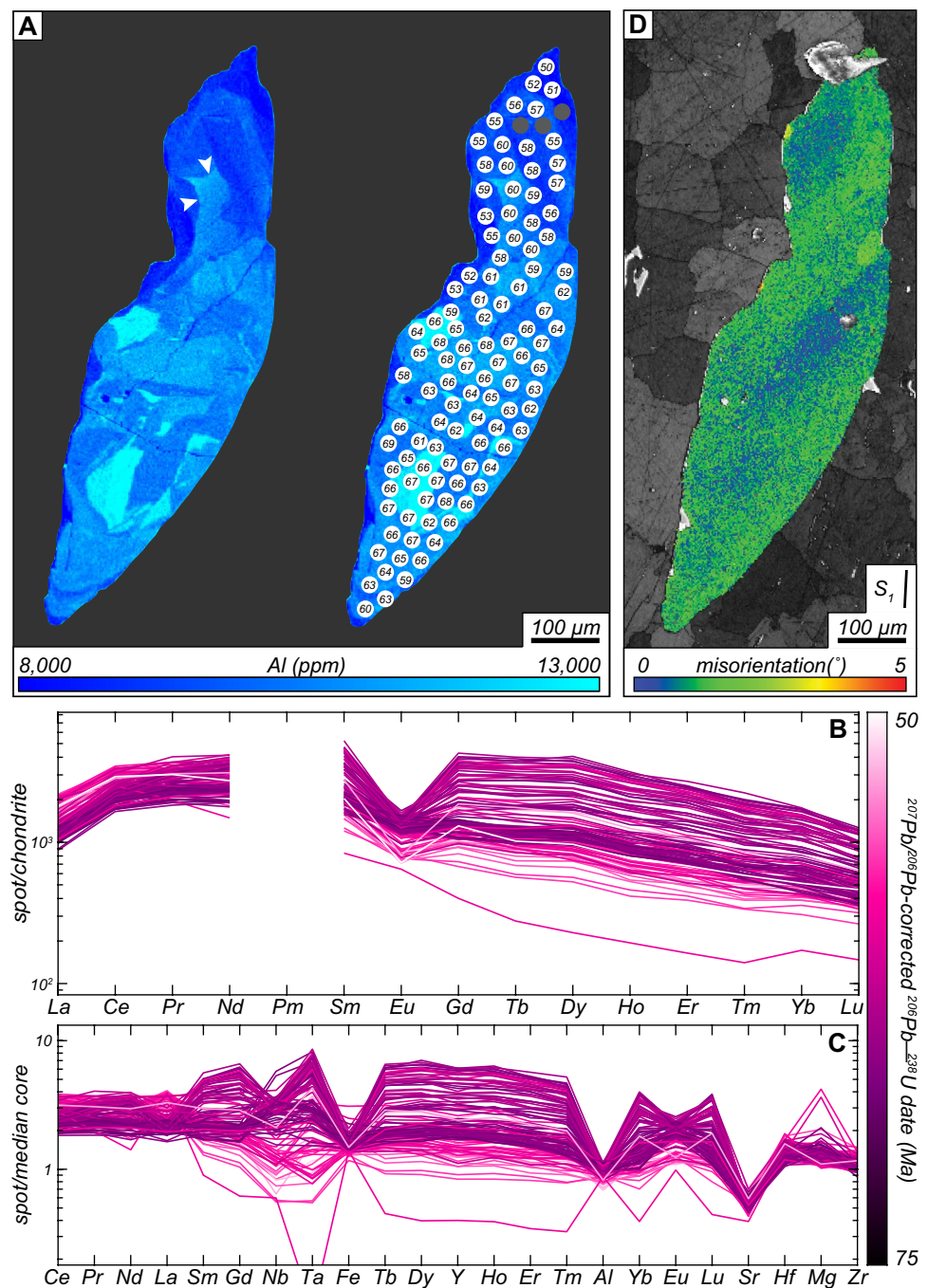


multiple fluids of different composition may have been present at the sample scale if they were sourced from the varying lithologies of the western metamorphic belt and the Great Tonalite Sill (e.g., Klepeis et al. 1998) and remained immiscible during metamorphism (Vard and Williams-Jones 1993; Romer et al. 2005; Heinrich 2007). Regardless of their scale or precise mechanism of their production, variable fluid compositions could explain the nonsystematic variations among date and trace-element concentrations within the dataset.

The composition of the fluid that drove titanite dissolution–reprecipitation must account for the mobilization of Zr, REEs, and Pb. REEs and high field strength elements (HFSE) like Zr are more soluble in aqueous solutions that contain fluorine (Keppler 1993; Pan and Fleet

1996; Hetherington et al. 2010; Rapp et al. 2010; Migdisov et al. 2011). The increasing La_N/Sm_N with younging date (Fig. 6B) and with increasing Zr-in-titanite temperature (Fig. S7) further supports an F-bearing fluid, as LREE-F⁺ aqueous compounds stabilize with increasing temperature (Migdisov et al. 2009). Carbonate-rich fluids also promote mobilization of the HFSE and REEs (Pouchon et al. 2001; Curti and Hummel, 1999), but the REEs complex more easily with carbonate anions than the HFSE (Chakhmouradian and Williams 2004), which is contrary to the mobilization of both the REEs and Zr that we observed. Further, high fluid X_{CO_2} in calcsilicates stabilizes rutile over titanite (Frost et al. 2000; Chakhmouradian and Williams 2004) and high Ca contents favor precipitation of fluorite (Salvi et al. 2000), but rutile and fluorite are absent from the studied sample.

Fig. 8 Undeformed titanite grain (grain 19) displaying patchy and lobate–cusate zoning, two of three zoning patterns observed in the dataset. **A** Al X-ray map, **B** chondrite-normalized REEs, **C** spider diagram of all measured trace elements normalized to the median dataset core values, and **D** misorientation map. Maximum and minimum concentrations in **A** were quantified using LASS data. Translucent white spots in **A** indicate the location of LASS analyses and the associated U–Pb dates (Ma). In-run date uncertainties from the dark gray spots are > 10% and were removed from the final dataset. In-run, 2σ uncertainties on U–Pb dates for this grain are ~ 2 Ma. White arrows in **A** denote lobate–cusate rim, compatible with dissolution–reprecipitation. Light rare-earth element, Zr, and Hf concentrations increase with younging date in this grain, whereas Al, Nb, and Ta concentrations decrease with younging date (**C, D**)

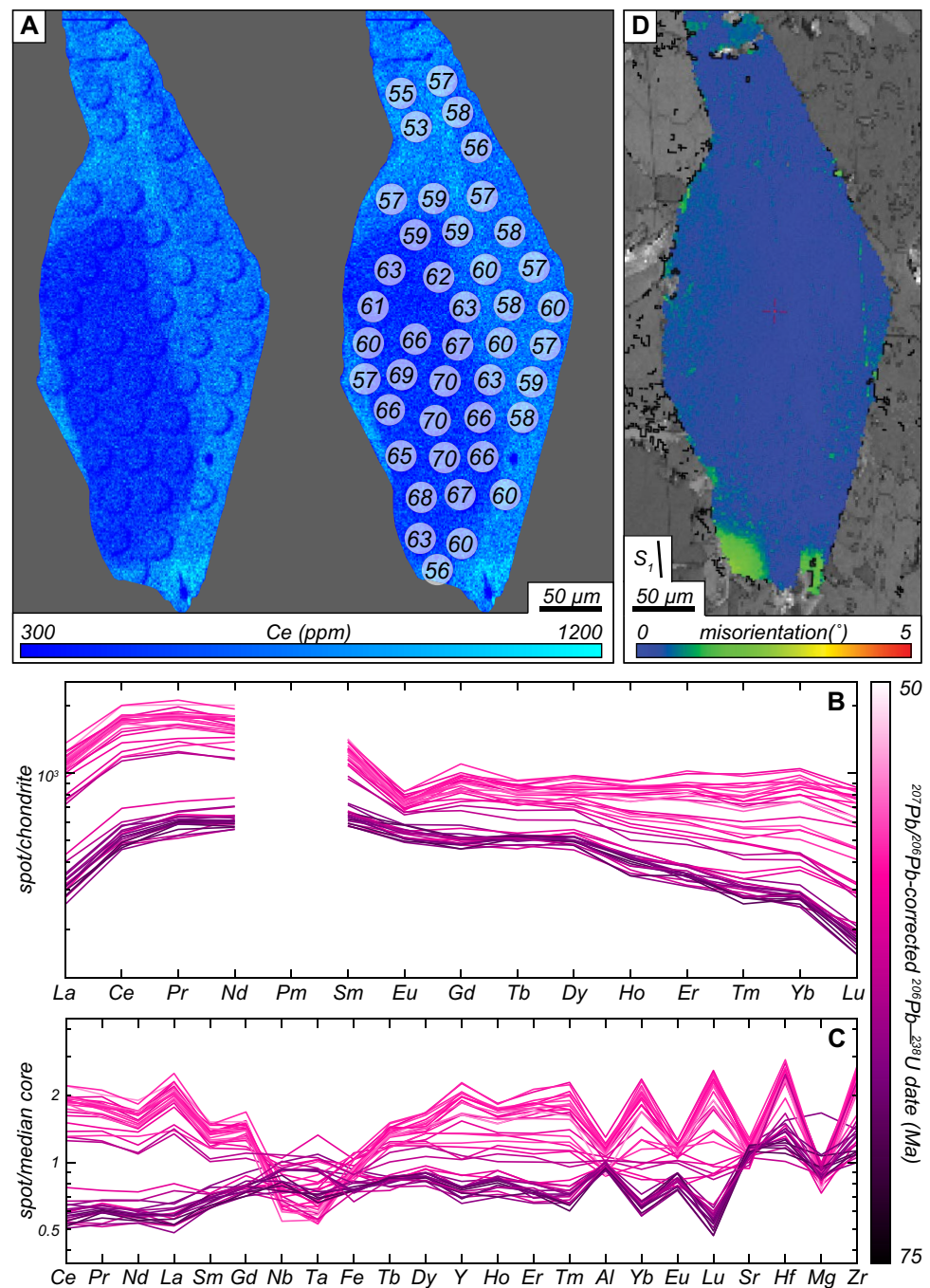


The absence of fluid inclusions in the analyzed titanite crystals preclude directly constraining the composition of the fluid(s) that recrystallized the grains. Further, to our knowledge, there are no experimental data on the fluid compositions associated with titanite dissolution–reprecipitation. Nevertheless, the data broadly support a metamorphic fluid that was likely an F-bearing, Ca-poor, H₂O-dominant CO₂-subservient mixture in which the relative proportions of F, H₂O, and CO₂ continually evolved as a result of dissolution–reprecipitation, producing variable relationships

between dates and trace-element concentrations within and among grains. Such a mixed H₂O–CO₂ metamorphic fluid is further supported by the presence of hydrous (amphibole, clinozoisite, biotite) and carbonate (calcite) minerals in the studied calcsilicate (Fig. 3).

The reason for the variable Pb removal from the grains is less clear. One potential explanation is that radiogenic Pb did not have a consistent oxidation state during recrystallization. For example, if radiogenic Pb was tetravalent, it would have behaved like a HFSE and have been relatively fluid immobile

Fig. 9 Undeformed titanite grain (grain 12) displaying core–rim zoning, one of three zoning patterns observed in the dataset. **A** Ce X-ray map, **B** chondrite-normalized REEs, **C** spider diagram of all measured trace elements normalized to the median dataset core values, and **D** misorientation map. Maximum and minimum concentrations in **A** were quantified using LASS data. Translucent white spots in **A** indicate the location of LASS analyses and the associated U–Pb dates (Ma). In-run, 2σ uncertainties on U–Pb dates for this grain are ~ 2 Ma. Rare-earth element, Y, Fe, Zr, and Hf concentrations increase with younging date in this grain (C, D). The geometrically simple rim revealed by the Ce X-ray map in **A** is interpreted to have resulted from dissolution–reprecipitation rather than secondary titanite growth



(Frei et al. 1997; Kramers et al. 2009) except in F-rich fluids (see above, Keppler 1993; Pan and Fleet 1996; Jiang et al. 2005; Hetherington et al. 2010; Rapp et al. 2010; Migdisov et al. 2011). On the other hand, if Pb was dominantly 2^+ , it would have behaved like a large-ion-lithophile element and be more soluble in a range of fluid compositions (Kramers et al. 2009). Direct constraints on the radiogenic Pb oxidation state in titanite, however, suggest that it is uniformly divalent (Syverson et al. 2019), making this explanation less plausible. Alternatively, radiation damage accumulation can

promote recrystallization by a diffusion–reaction process (Rizvanova et al. 2000; Davis and Krough 2000; Geisler et al. 2007), and variable degrees of radiation damage among the analyzed grains might have driven differential removal of Pb. This hypothesis is permissible if some of the titanite grains are detrital (see “Discussion”), but if the oldest titanite date reflects the onset of metamorphic titanite crystallization, the temperatures would have been too high to permit significant radiation damage accumulation (c.f. Coyle and Wagner 1998). Instead, we suggest that the decoupled dates

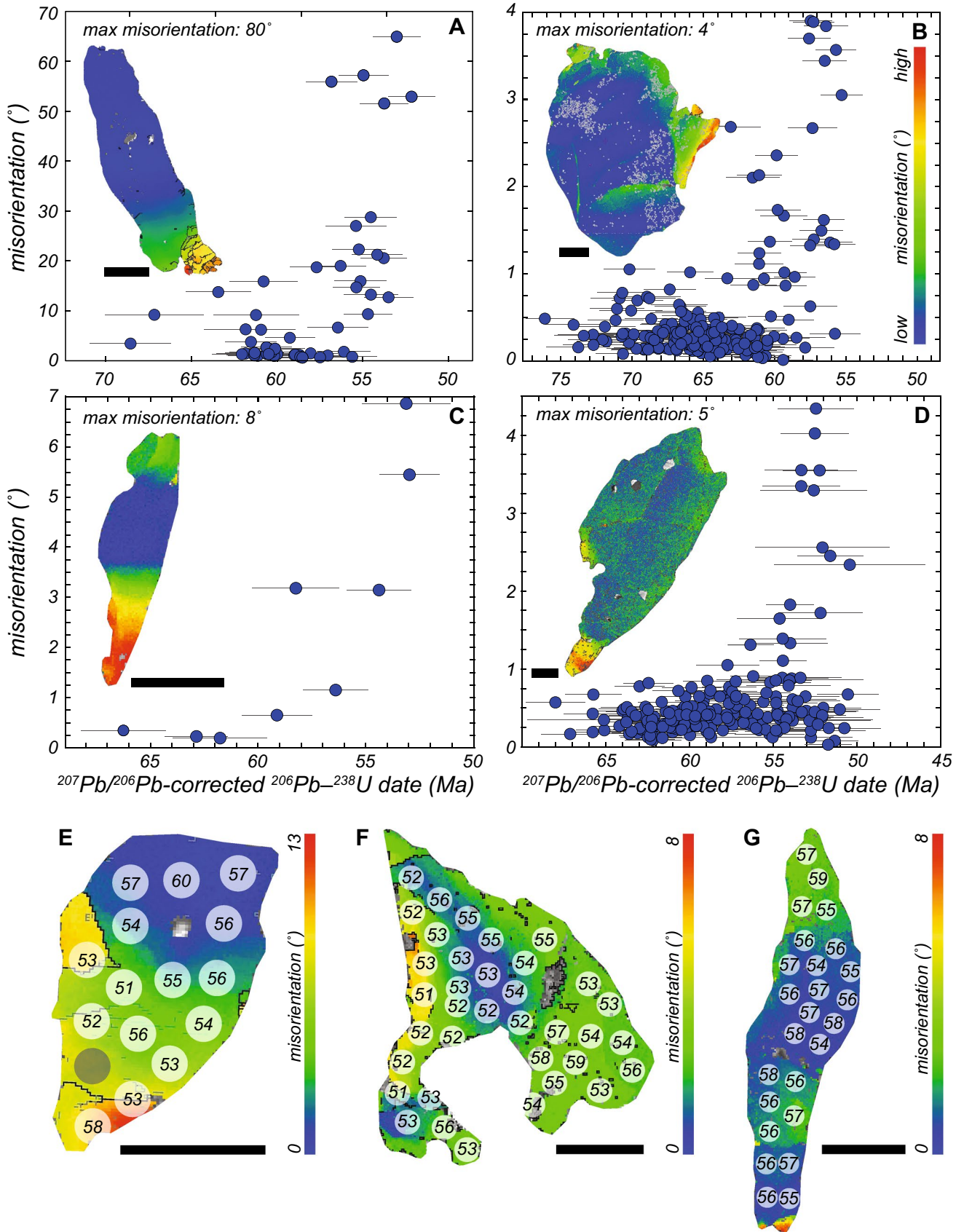


Fig. 10 EBSD maps and dates for the seven bent titanite grains. **A–D** Date vs. misorientation plots and EBSD maps for the four bent grains wherein dates young with increasing lattice bending: **A** grain 7, **B** grain 3, **C** grain 2, and **D** grain 18. EBSD scale in **B** applies to all maps in **A–D**. **E–G** EBSD maps and dates from the three bent grains that yield dates exclusively younger than 60 Ma. **E** grain 4, **F** grain 13, and **G** grain 17. White circles indicate location of laser ablation analyses with the corresponding date (Ma). Gray spot in **E** yielded a date with > 10% in-run uncertainty that was removed from the final dataset. In-run date uncertainties are ~5% for grain 4 (**E**), ~4% for grain 13 (**F**), and ~4% for grain 17 (**G**). Black lines are low-angle subgrain boundaries. All black scale bars in (**A–G**) are 100 μm

and trace-element contents may reflect the remobilization but not removal of radiogenic Pb during dissolution–reprecipitation, giving host to “parentless daughter”, as has been proposed for some fluid-affected zircon (Hoskin and Black 2000; Carson et al. 2002; Kusiak et al. 2013; Weinberg et al. 2020). However, why this phenomenon occurred in some grains and not others cannot be resolved with our data, but it may be linked to the likely variable fluid compositions at the thin-section scale as discussed above.

Deformation

Four titanite grains have ~4–80° of lattice misorientation with respect to a central reference point (“bent grains”), low-angle boundaries at grain tips, and U–Pb dates that span the entire ~75–50 Ma range of the dataset (Table 1; Fig. 10A–D). Dates young with increasing lattice bending in these crystals, with the youngest dates (~60–50 Ma) in the rotated grain tips and subgrains (Fig. 10A–D). This relationship suggests that the dates from bent grain tips record the timing of crystal-plastic deformation. Three additional titanite grains display ~8–12° of total intragrain misorientation, have low-angle grain boundaries, and yield no U–Pb dates older than ~60 Ma (Table 1; Fig. 10E–G). Further, it is only in bent grains where this more restricted range in dates is observed. This implies that the U–Pb dates from these grains were completely reset as a result of the lattice bending that accommodated deformation.

We note that the evidence for dissolution–reprecipitation makes it difficult to unequivocally interpret that the ~60–50 Ma dates from the bent grains record the timing of lattice bending (deformation) rather than fluid-mediated recrystallization. Two of the bent grains (grains 3 and 18; Fig. 10B, D) have ~60–50 Ma dates in unbent parts of the grain; these young dates likely reflect the timing of interface-coupled dissolution–reprecipitation, rather than lattice bending. Additionally, U–Pb dates are positively or negatively correlated with some trace-elements in two of the bent grains (grains 2 and 18; Figs. S5B, S5R), consistent with date resetting by interface-coupled dissolution–reprecipitation rather than lattice bending. Nevertheless, there is always a relationship between microstructure and date in bent grains: dates

either young with increasing misorientation or all dates are younger than 60 Ma (Fig. 10). Despite the evidence for dissolution–reprecipitation, these consistent patterns between dates and microstructure suggests that lattice bending played a role in resetting the U–Pb dates in the bent grains.

The gradational nature of lattice bending and the low-angle subgrain boundaries (Fig. 10) implies that these deformation microstructures formed from the production and motion of dislocations within the titanite. If these are dislocation-related microstructures, and the development of these microstructures played a role in resetting the U–Pb dates, this suggests that dislocations and low-angle boundaries facilitated Pb loss from the titanite. However, we cannot unequivocally invoke the role of dislocations in resetting U–Pb dates given the analytical scale of the dataset. Further, the only existing nanoscale observations of dislocations in titanite show no change in Pb concentration within or across low-angle grain boundaries (Kirkland et al. 2018), implying that in some instances, dislocation-facilitated diffusion (i.e., pipe diffusion and Cottrell Atmospheres) may not affect Pb. We suggest that deformed titanite whose microstructures yield young dates are promising candidates for future studies aimed at constraining the mechanisms and complexities of dislocation-facilitated Pb loss in titanite.

Coupled deformation and dissolution–reprecipitation

As discussed above, the superposition of lattice bending and low-angle boundaries on fluid-related zoning makes it difficult to differentiate the roles that deformation and fluid-mediated recrystallization played in resetting the titanite U–Pb dates. In addition, the trace-element compositions of the three grains whose dates we interpret to have been completely reset by deformation (Fig. 10E–G) overlap the range of compositions from the undeformed, fluid-recrystallized rims (Fig. S8). This suggests that the trace-element signatures of the three deformed, completely reset grains were affected by the same fluids that produced the lobate–cusped rims in other grains. Further, it is only in the bent grains that the trace-element contents appear to be reset across the entire grain and not just at grain margins. These two observations imply that lattice bending and dissolution–reprecipitation were coupled processes that together worked to reset dates and trace-element signatures in the bent grains. We suggest that microstructures provided fast diffusion pathways that facilitated isotopic and trace-element exchange between the fluid and grain interiors in the bent grains, similar to the role porosity has been suggested to play in dissolution–reprecipitation reactions (Putnis 2009). The resetting of U–Pb dates by lattice bending, therefore, was likely never independent of fluid alteration in these titanite.

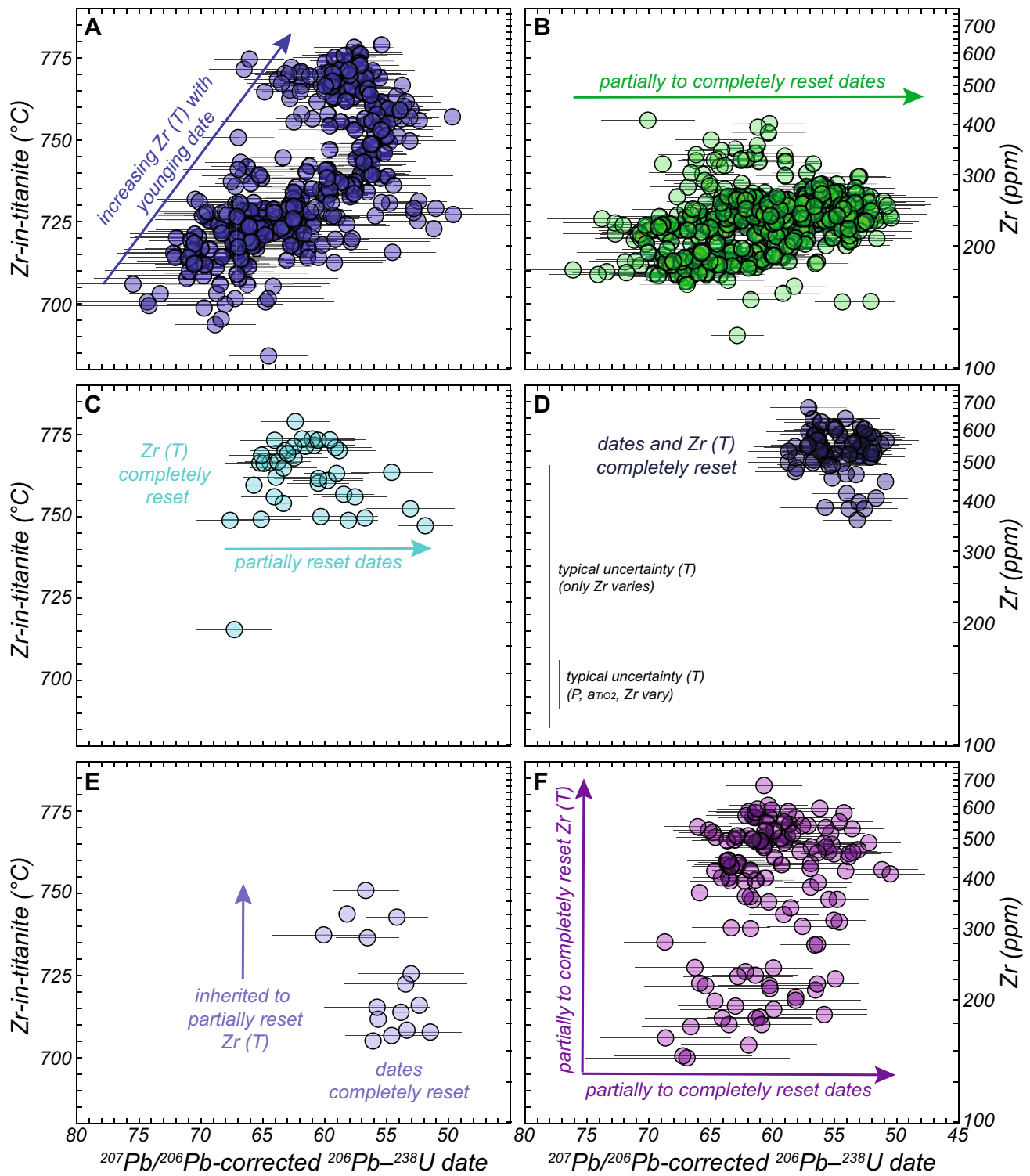


Fig. 11 Date vs. Zr-in-titanite temperature for **A** titanite wherein Zr increases with younging date (9 grains), **B** titanite with Zr-in-titanite temperatures ~700–730 °C (3 grains), **C** grains with Zr-in-titanite temperatures ~750–775 °C (three grains), **D** bent titanite grains with <60 Ma dates and ~750–775 °C Zr-in-titanite temperatures (2

grains), **E** a single grain with <60 Ma dates and variable Zr contents, and **F** completely scattered dates and Zr-in-titanite temperatures from three grains. In aggregate, these six patterns have apparently bimodal Zr-in-titanite temperatures at the scale of the entire dataset. Representative temperature uncertainties indicated in **D** apply to all plots

Timing of deformation and dissolution–reprecipitation

Dates from the bent grain tips, subgrains, and crystals we interpret to have been completely reset from deformation range from ~60 to 50 Ma (Fig. 12A). The weighted mean of these dates is 55 ± 1 Ma (MSWD = 2.6; Fig. 12A). These data are consistent with either ~10 Myr of continuous deformation or a range of partial to complete resetting of dates during a discrete deformation event. Ten million years of deformation would be compatible with previous interpretations that the Coast shear zone was active from ~65 to 55 Ma (Klepeis et al. 1998). However, without more detailed work on the effects of crystal-plastic deformation on elemental mobility in titanite, it is not possible to differentiate between a protracted deformation history or partial to complete resetting of dates during deformation. We, therefore, suggest that these titanites were almost certainly deforming around 55 Ma, and that deformation may have begun as early as 60 Ma and ended as late as 50 Ma.

We constrain the timing of interface-coupled dissolution–reprecipitation using the dates from the fluid-recrystallized rims wherein dates young with increasing Ce concentration (11 grains, see Table 1). The consistent relationship between dates and Ce concentrations in these grains suggests that these rim dates accurately reflect the timing of fluid-mediated recrystallization. Similar to the bent titanite, dates from the fluid-recrystallized rims largely range from ~60 to 50 Ma (Fig. 12B). The weighted mean of dates from the recrystallized rims is 58 ± 1 Ma (MSWD of 5.7; Fig. 12B). The spread in dates and high MSWD imply either ~10 Myr of dissolution–reprecipitation reactions, or partial to complete resetting of the U–Pb system during a discrete event (e.g., Kelly et al. 2012). It is not possible to discriminate between these two interpretations; we conservatively suggest that 60 Ma is the maximum onset of titanite dissolution–reprecipitation, that these reactions were likely ongoing at 58 Ma, and that fluid-mediated recrystallization ceased by 50 Ma.

The timing of initial titanite crystallization is constrained by dates from grain cores wherein dates young with increasing Ce concentration (11 grains, see Table 1). The consistent relationships between dates and Ce concentrations in these grains suggest that dates from these cores were least affected by fluid-mediated recrystallization and are most likely to faithfully record the timing of crystallization. Dates in the cores of the fluid-recrystallized titanite range from ~75 to 60 Ma with a weighted mean of 64 Ma (MSWD = 5.5; Fig. 12C). The spread in dates and large MSWD suggests either 15 Myr of continuous titanite crystallization (e.g., Stearns et al. 2016), partial fluid-mediated resetting of titanite that crystallized at 75 Ma, or detrital cores with crystallization ages significantly older than 75 Ma that were partially reset at ~60–50 Ma. It is not possible to differentiate among

these interpretations of the oldest titanite dates given the current data. We therefore suggest that titanite neocrystallization ceased by 60 Ma.

Implications for titanite petrochronology

The twenty analyzed titanite grains and their associated U–Pb dates, zoning, trace-element composition, and microstructures preserve evidence for simultaneous interface-coupled dissolution–reprecipitation and lattice bending within a single sample. These data highlight the range of processes that can be recorded by titanite grains subjected to the same metamorphic and deformation history at the scale of a single thin section. The workflow presented herein demonstrates the potential complexities in titanite U–Pb dates, and how careful comparison of date with distance from the grain edge, trace-element composition, zoning, and microstructure makes it possible to link those dates to multiple, simultaneous processes affecting titanite chemistry. Our efforts further show that sample-scale date and chemical trends may be misleading: our full titanite dataset shows that there are very few robust sample-scale trends despite the prevalence of clear correlations within individual grains, and indicate chemical heterogeneity on sub-grain, grain, and thin-section scales that might not be evident without detailed, grain-scale analyses.

The highly variable, unsystematic coupling–decoupling of U–Pb dates and trace-element contents observed in the titanite grains in this study, and of titanite and other accessory minerals (zircon, monazite) elsewhere in the literature, is an increasingly recognized phenomenon that apparently results from some combination of fluid alteration, volume diffusion of U and/or Pb, and deformation (Kunz et al. 2018; Garber et al. 2020a; Weinberg et al. 2020; Gordon et al. 2021). The microtextural evidence of dissolution–reprecipitation presented here implies that U–Pb date and trace-element decoupling in the Coast shear zone titanite was driven by differences in the chemical potentials of trace elements and Pb between the titanite and the metamorphic fluid (Putnis and Mezger 2004; Putnis 2005, 2009), and that these controls never achieved equilibrium on the thin-section scale.

Although many advances have been made in the past decade (Moser et al. 2009; MacDonald et al. 2013; Bonamici et al. 2015; Piazzolo et al. 2016; Kovaleva et al. 2017; Langone et al. 2017; Papapavlou et al. 2018; Moore et al. 2020; Fougereuse et al. 2021; Gordon et al. 2021), directly dating crystal-plastic deformation, fluid flow, and other processes associated with slip along ductile shear zones remains challenging. Titanite U–Pb dates are correlated with deformation microstructures in our dataset—bent grains, bent grain tips, and subgrains have the youngest dates—but the evidence for dissolution–reprecipitation makes it difficult to specify

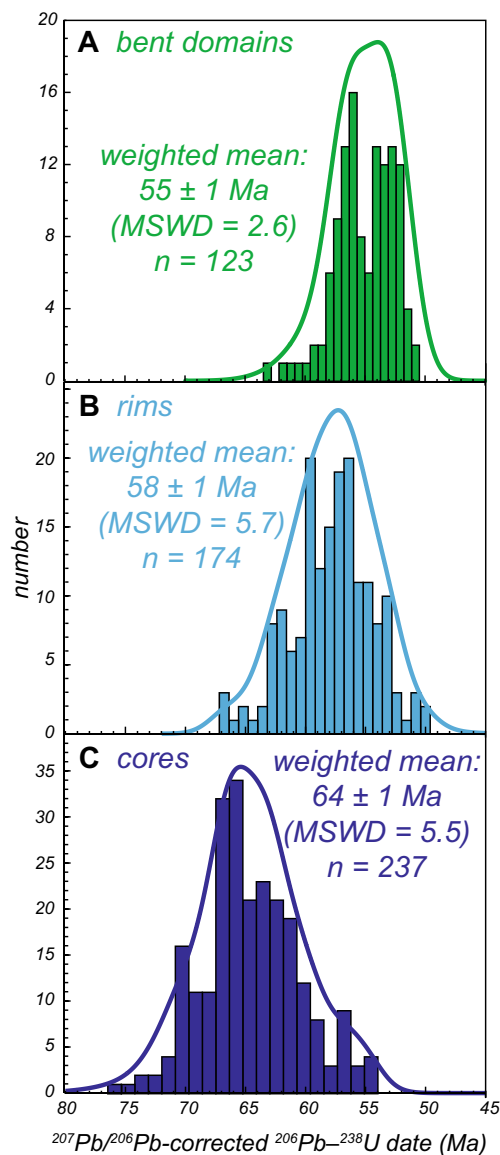


Fig. 12 Probability density functions, histograms, and weighted mean values for **A** bent domains, **B** fluid-recrystallized rims, and **C** grain cores. Dates included in **A** comprise dates from bent grain tips in grains 2, 3, 7, and 18, as well as all dates from grains 4, 13, and 17 (see Table S2). Dates included in **B** and **C** are rim and core values from the 11 grains that yielded increasing Ce concentration with younging date (see Tables 1 and S2)

an unequivocal deformation age. Still, these data contribute to a growing body of work demonstrating that titanite is a promising candidate to directly date crystal-plastic deformation (Bonamici et al. 2015; Papapavlou et al. 2018; Gordon et al. 2021) and fluid flow (Garber et al. 2017; Holder and Hacker 2019).

Zr-in-titanite data (this study) and prior constraints on metamorphic temperatures of Coast shear zone metapelites (Klepeis et al. 1998) suggest that the analyzed Coast shear

zone titanite resided at > 700 °C for ~ 25 Myr, yet the crystals show no conclusive evidence for volume diffusion of Pb at the titanite grain scale. Although we cannot rule out volume diffusion at lengthscales less than $25 \mu\text{m}$, our results are nonetheless compatible with the previously published conclusions that Pb volume diffusion in titanite at < 750 °C may be negligible (Stearns et al. 2016; Kohn 2017; Holder et al. 2019). Our data support the notion that titanite U–Pb dates should not be interpreted as cooling ages in the absence of spatial information supporting that contention.

Implications for the tectonometamorphic history of the Coast shear zone

Coast shear zone titanite U–Pb dates in combination with trace-element concentrations, Zr-in-titanite temperatures, zoning, and microstructures suggest that intrusion of the Great Tonalite Sill caused simultaneous heating, fluid alteration and deformation of the country rocks. The fluid-recrystallized titanite rims with elevated Zr and REE contents and their associated ~ 60 – 50 Ma dates in the studied sample (Figs. 7, 8, 9, 11A, 12B) likely record heating and igneous or metamorphic fluid influx associated with these intrusions (Hayden et al. 2008), although these data may alternatively reflect the combined effects of exhumation and heating during intrusion of the Great Tonalite Sill (e.g., Wood et al. 1991; Klepeis et al. 1998). The increase in temperature at ~ 60 Ma may reflect advective fluid pulses or conductive heating from the Sill, but the precise cause is unknown.

Zircon crystallization ages from deformed and undeformed intrusions suggest that the Coast shear zone near Portland Inlet was active from ~ 65 to 55 Ma but do not preclude deformation in the westernmost Coast shear zone, from which the sample analyzed herein is from, after this time (Klepeis et al. 1998). U–Pb dates from the bent titanite grains and grain tips are consistently ~ 60 – 50 Ma (Figs. 10, 12), implying that these data record titanite deformation during Coast shear zone slip. If this range reflects 10 Myr of continuous deformation, this suggests that the metasedimentary rocks west of the Great Tonalite Sill (Fig. 2B) deformed as late as ~ 50 Ma, 5 Myr after the end of Great Tonalite Sill magmatism and 5 Myr later than previously suggested (Klepeis et al. 1998). This interpretation is consistent with the conclusion that the youngest phase of Coast shear zone deformation was concentrated in a ~ 1 – 2 km zone west of the Sill (Klepeis et al. 1998). Alternatively, our interpretation that the titanite were likely deforming at ~ 55 Ma (see “Timing of deformation and dissolution–reprecipitation”) is consistent with the notion that ductile deformation along the Coast shear zone ended around this time (Klepeis et al. 1998).

Conclusions

Integrated U–Pb, trace-element, zoning, and microstructural data from twenty titanite crystals deformed in the Coast shear zone demonstrate that the grains were modified by two metamorphic processes—interface-coupled dissolution–reprecipitation and lattice bending that accommodated deformation—at the scale of a single thin section. Dates from lobate–cusped rims, bent grains and grain tips, and subgrains range from ~60 to 50 Ma, suggesting up to 10 Myr of fluid-mediated recrystallization and date resetting via lattice bending. These data are consistent with the onset of concomitant deformation, fluid-flow, and heating and/or exhumation from intrusion of the Great Tonalite Sill and slip along the Coast shear zone by ~60 Ma. Deformation and fluid-flow within the shear zone may have been ongoing as late as ~50 Ma.

Extremely variable correlations between titanite U–Pb dates and trace-elements imply thin section- or even grain-scale differences in the composition of the fluid driving dissolution–reprecipitation. The decoupling of U–Pb dates and trace elements in some of the unbent, fluid-recrystallized titanite further suggests that the relative compatibilities of Pb and trace elements in a mixed H₂O–CO₂ fluid drove differential date–composition decoupling during dissolution–reprecipitation. Deformation microstructures are superimposed on fluid-recrystallized rims, implying that these two processes were coupled at the grain scale and that microstructures may have provided pathways for fluids to reach the reaction front. Although the evidence for fluids and deformation in the same thin section precludes an unambiguous interpretation of the deformation age, titanite remains a promising candidate to directly date both crystal-plastic deformation and fluid flow.

Supplementary Information The online version contains supplementary material available at <https://doi.org/10.1007/s00410-022-01906-9>.

Acknowledgements This work was funded by NSF-EAR 1927060 to BRH, NSF-EAR 1928337 to GEG, and an MSA Grant for Student Research to ACM. We thank Robert Holder for help with data reduction and treatment and Matthew Rioux for discussions that improved our interpretation of the dataset. Ryan Stoner and Devin Rand helped with processing the data in MATLAB. We are grateful to Chris Kirkland, an anonymous reviewer, and associate editor Daniela Rubatto, whose comments improved the manuscript.

Funding This work was funded by NSF-EAR 1927060 to BRH, NSF-EAR 1928337 to GEG, and an MSA Grant for Student Research to ACM.

Data availability Chronology data are currently being archived in the FAIR-compliant Geochron data repository that will be made publicly available on publication of this manuscript.

Declarations

Conflict of interest The authors declare that there are no known conflicts of interest that have affected the data and interpretations presented herein.

Open Access This article is licensed under a Creative Commons Attribution 4.0 International License, which permits use, sharing, adaptation, distribution and reproduction in any medium or format, as long as you give appropriate credit to the original author(s) and the source, provide a link to the Creative Commons licence, and indicate if changes were made. The images or other third party material in this article are included in the article's Creative Commons licence, unless indicated otherwise in a credit line to the material. If material is not included in the article's Creative Commons licence and your intended use is not permitted by statutory regulation or exceeds the permitted use, you will need to obtain permission directly from the copyright holder. To view a copy of this licence, visit <http://creativecommons.org/licenses/by/4.0/>.

References

- Aleinikoff JN, Wintsch RP, Tollo RP et al (2007) Ages and origins of rocks in the Killingworth Dome, South-central Connecticut: Implications for the tectonic evolution of southern New England. *Am J Sci* 307:63–118. <https://doi.org/10.2475/01.2007.04>
- Andronicos CL, Chardon DH, Hollister LS et al (2003) Strain partitioning in an obliquely convergent orogen, plutonism, and synorogenic collapse: coast Mountains Batholith, British Columbia Canada. *Tectonics*. <https://doi.org/10.1029/2001TC001312>
- Austrheim H (1987) Eclogitization of lower crustal granulites by fluid migration through shear zones. *Earth Planet Sci Lett* 81:221–232
- Bonamici CE, Fanning CM, Kozdon R et al (2015) Combined oxygen-isotope and U–Pb zoning studies of titanite: new criteria for age preservation. *Chem Geol* 398:70–84. <https://doi.org/10.1016/j.chemgeo.2015.02.002>
- Budzyń B, Harlov DE, Williams M, Jercinovic MJ (2011) Experimental determination of stability relations between monazite, fluorapatite, allanite, and REE-epidote. *Am Mineral* 96:1547–1567. <https://doi.org/10.2138/am.2011.3741>
- Carson CJ, Ague JJ, Grove M et al (2002) U–Pb isotopic behaviour of zircon during upper-amphibolite facies fluid infiltration in the Napier Complex, east Antarctica. *Earth Planet Sci Lett* 199:287–310
- Chakhmouradian AR, Williams CT (2004) Mineralogy of high field strength elements (Ti, Nb, Zr, Ta, Hf) in phoscorite and carbonatitic rocks of the Kola Peninsula, Russia. In: Wall F, Zaitsev AN (eds) Phoscorites and carbonatites from mantle to mine: the key example of the Kola Alkaline Province. *The Mineralogical Society of Great Britain & Ireland*, London, pp 293–340
- Chambers JA, Kohn MJ (2012) Titanium in muscovite biotite, and hornblende: modeling, thermometry, and rutile activities of metapelites and amphibolites. *Am Mineral* 97:543–555. <https://doi.org/10.2138/am.2012.3890>
- Cherniak DJ (1993) Lead diffusion in titanite and preliminary results on the effects of radiation damage on Pb transport. *Chem Geol* 110:177–194. [https://doi.org/10.1016/0009-2541\(93\)90253-F](https://doi.org/10.1016/0009-2541(93)90253-F)
- Cherniak DJ (1995) Sr and Nd diffusion in titanite. *Chem Geol* 125:219–232
- Cottrell AH, Bilby BA (1949) Dislocation theory of yielding and strain ageing of iron. *Proc Phys Soc* 62:49–62

- Coyle DA, Wagner GA (1998) Positioning the titanite fission-track partial annealing zone. *Chem Geol* 149:117–125
- Crank J (1975) The mathematics of diffusion. Brunel University Press
- Crawford ML, Hollister LS (1982) Contrast of metamorphic and structural histories across the work channel lineament, Coast Plutonic Complex, British Columbia. *J Geophys Res* 87:3849–3860
- Crawford ML, Hollister LS, Woodsworth GJ (1987) Crustal deformation and regional metamorphism across a terrane boundary, Coast Plutonic Complex, British Columbia. *Tectonics* 6:343–361. <https://doi.org/10.1029/TC006i003p00343>
- Curti E, Hummel W (1999) Modeling the solubility of zirconia in a repository for high-level radioactive waste. *J Nucl Mater* 274:189–196
- Davis DW, Krogh TE (2000) Preferential dissolution of ²³⁴U and radiogenic Pb from a-recoil-damaged lattice sites in zircon: implications for thermal histories and Pb isotopic fractionation in the near surface environment. *Chem Geol* 172:41–58
- Dodson MH (1973) Closure temperature in cooling geochronological and petrological systems. *Contrib Mineral Petrol* 40:259–274
- Fossen H, Tikoff B (1998) Extended models of transpression and transtension, and application to tectonic settings. *Geol Soc London, Spec Publ* 135:15–33
- Fougerouse D, Reddy SM, Kirkland CL et al (2019) Time-resolved, defect-hosted, trace element mobility in deformed Witwatersrand pyrite. *Geosci Front* 10:55–63. <https://doi.org/10.1016/j.gsf.2018.03.010>
- Fougerouse D, Reddy SM, Kirkland CL et al (2021) Mechanical twinning of monazite expels radiogenic lead. *Geology* 49:417–421. <https://doi.org/10.1130/G48400.1>
- Frei R, Villa I, Nagler TF et al (1997) Single mineral dating by the Pb–Pb step-leaching method: assessing the mechanisms. *Geochim Cosmochim Acta* 61:393–414
- Frost BR, Chamberlain KR, Schumacher JC (2000) Sphene (titanite): phase relations and role as a geochronometer. *Chem Geol* 172:131–148. [https://doi.org/10.1016/S0009-2541\(00\)00240-0](https://doi.org/10.1016/S0009-2541(00)00240-0)
- Garber JM, Hacker BR, Kylander-Clark ARC et al (2017) Controls on trace element uptake in metamorphic titanite: Implications for petrochronology. *J Petrol* 58:1031–1057. <https://doi.org/10.1093/petrology/egx046>
- Garber JM, Smye AJ, Feineman MD et al (2020a) Decoupling of zircon U–Pb and trace-element systematics driven by U diffusion in eclogite-facies zircon (Monviso meta-ophiolite, W. Alps). *Contrib Mineral Petrol* 175:1–25. <https://doi.org/10.1007/s00410-020-01692-2>
- Garber JM, Rioux M, Clark ARCK et al (2020b) Petrochronology of wadi tayin metamorphic sole metasediment, with implications for the thermal and tectonic evolution of the Samail Ophiolite (Oman/UAE). *Tectonics* 39:1–28. <https://doi.org/10.1029/2020TC006135>
- Gehrels GE, McClelland WC, Samson SD et al (1991) U–Pb geochronology of late Cretaceous and early Tertiary plutons in the northern Coast Mountains Batholith. *Can J Earth Sci* 28:899–911. <https://doi.org/10.1139/e91-082>
- Geisler T, Pidgeon RT, Kurtz R et al (2003) Experimental hydrothermal alteration of partially metamict zircon. *Am Mineral* 88:1496–1513
- Geisler T, Schaltegger U, Tomaschek F (2007) Re-equilibration of zircon in aqueous fluids and melts. *Elements* 3:43–50. <https://doi.org/10.2113/gselements.3.1.43>
- Ghent ED, Stout MZ (1984) TiO₂ activity in metamorphosed pelitic and basic rocks: principles and applications to metamorphism in southeastern Canadian Cordillera. *Contrib Mineral Petrol* 86:248–255. <https://doi.org/10.1007/BF00373670>
- Goncalves P, Oliot E, Marquer D, Connolly JAD (2012) Role of chemical processes on shear zone formation: an example from the Grimsel metagranodiorite (Aar massif, Central Alps). *J Metamorph Geol* 30:703–722. <https://doi.org/10.1111/j.1525-1314.2012.00991.x>
- Gordon SM, Kirkland CL, Reddy SM et al (2021) Deformation-enhanced recrystallization of titanite drives decoupling between U–Pb and trace elements. *Earth Planet Sci Lett* 560:116810. <https://doi.org/10.1016/j.epsl.2021.116810>
- Hacker BR, Kylander-Clark ARC, Holder R et al (2015) Monazite response to ultrahigh-pressure subduction from U–Pb dating by laser ablation split stream. *Chem Geol* 409:28–41. <https://doi.org/10.1016/j.chemgeo.2015.05.008>
- Harlov DE, Wirth R, Hetherington CJ (2011) Fluid-mediated partial alteration in monazite: the role of coupled dissolution–recrystallization in element redistribution and mass transfer. *Contrib Mineral Petrol* 162:329–348. <https://doi.org/10.1007/s00410-010-0599-7>
- Harrison TM, Armstrong RL, Naeser CW, Harakal JE (1979) Geochronology and thermal history of the Coast Plutonic Complex, near Prince Rupert, British Columbia. *Can J Earth Sci* 16:400–410. <https://doi.org/10.1139/e79-038>
- Hart EW (1957) On the role of dislocations in bulk diffusion. *Acta Metall* 5:597
- Hartnady MI, Kirkland CL, Clark C et al (2019) Titanite dates crystallization: slow Pb diffusion during super-solidus re-equilibration. *J Metamorph Geol* 37:823–838. <https://doi.org/10.1111/jmg.12489>
- Hayden LA, Watson EB, Wark DA (2008) A thermobarometer for sphene (titanite). *Contrib Mineral Petrol* 155:529–540. <https://doi.org/10.1007/s00410-007-0256-y>
- Heinrich W (2007) Fluid immiscibility in metamorphic rocks. *Rev Mineral Geochem* 65:389–430
- Hetherington CJ, Harlov DE, Budzyń B (2010) Experimental metasomatism of monazite and xenotime: mineral stability, REE mobility and fluid composition. *Mineral Petrol* 99:165–184. <https://doi.org/10.1007/s00710-010-0110-1>
- Hirth G, Tullis J (1991) Dislocation creep regimes in quartz aggregates. *J Struct Geol* 14:145–159. [https://doi.org/10.1016/0191-8141\(92\)90053-Y](https://doi.org/10.1016/0191-8141(92)90053-Y)
- Hoffman R (1956) Anisotropy of grain boundary self-diffusion. *Acta Metall* 4:97–98
- Holder RM, Hacker BR (2019) Fluid-drive resetting of titanite following ultrahigh-temperature metamorphism in southern Madagascar. *Chem Geol* 504:38–52. <https://doi.org/10.1016/j.chemgeo.2018.11.017>
- Holder RM, Hacker BR, Seward GGE, Kylander ARC (2019) Interpreting titanite U–Pb dates and Zr thermobarometry in high-grade rocks: empirical constraints on elemental diffusivities of Pb, Al, Fe, Zr, Nb, and Ce. *Contrib Mineral Petrol* 174:1–19. <https://doi.org/10.1007/s00410-019-1578-2>
- Hollister LS (1970) Origin, Mechanism, and consequences of compositional sector zoning in staurolite. *Am Mineral* 55:742–766
- Hollister LS, Crawford ML (1986) Melt-enhanced deformation: a major tectonic process. *Geology* 14:558–561. [https://doi.org/10.1130/0091-7613\(1986\)14%3c558:MDAMTP%3e2.0.CO](https://doi.org/10.1130/0091-7613(1986)14%3c558:MDAMTP%3e2.0.CO)
- Hoskin PWO, Black LP (2000) Metamorphic zircon formation by solid-state recrystallization of protolith igneous zircon. *J Metamorph Geol* 18:423–439
- Huang J, Meyer M, Pontikis V (1989) Is pipe diffusion in metals vacancy controlled? A molecular-dynamics study of an edge dislocation in copper. *Phys Rev Lett* 63:628–631
- Ingram GM, Hutton DHW (1994) The Great Tonalite Sill: emplacement into a contractional shear zone and implications for late Cretaceous to early Eocene tectonics in southeastern Alaska and British Columbia. *Geol Soc Am Bull* 106:715–728. [https://doi.org/10.1130/0016-7606\(1994\)106%3c0715:TGTSEI%3e2.3.CO;2](https://doi.org/10.1130/0016-7606(1994)106%3c0715:TGTSEI%3e2.3.CO;2)

- Jamtveit B, Austrheim H, Putnis A (2016) Disequilibrium metamorphism of stressed lithosphere. *Earth Sci Rev* 154:1–13. <https://doi.org/10.1016/j.earscirev.2015.12.002>
- Jiang SY, Wang RC, Xu XS, Zhao KD (2005) Mobility of high field strength elements (HFSE) in magmatic-, metamorphic-, and submarine-hydrothermal systems. *Phys Chem Earth* 30:1020–1029. <https://doi.org/10.1016/j.pce.2004.11.004>
- Kapp P, Manning CE, Tropper P (2009) Phase-equilibrium constraints on titanite and rutile activities in mafic epidote amphibolites and geobarometry using titanite–rutile equilibria. *J Metamorph Geol* 27:509–521. <https://doi.org/10.1111/j.1525-1314.2009.00836.x>
- Kelly NM, Harley SL, Möller A (2012) Complexity in the behavior and recrystallization of monazite during high-T metamorphism and fluid in filtration. *Chem Geol* 322–323:192–208. <https://doi.org/10.1016/j.chemgeo.2012.07.001>
- Keppeler H (1993) Influence of fluorine on the enrichment of high field strength trace elements in granitic rocks. *Contrib Mineral Petrol* 114:479–488
- Kirkland CL, Spaggiari CV, Johnson TE et al (2016) Grain size matters: implications for element and isotopic mobility in titanite. *Precambrian Res* 278:283–302. <https://doi.org/10.1016/j.precamres.2016.03.002>
- Kirkland CL, Fougereuse D, Reddy SM et al (2018) Assessing the mechanisms of common Pb incorporation into titanite. *Chem Geol* 483:558–566. <https://doi.org/10.1016/j.chemgeo.2018.03.026>
- Klepeis KA, Crawford ML, Gehrels G (1998) Structural history of the crustal-scale Coast shear zone north of Portland Canal, southeast Alaska and British Columbia. *J Struct Geol* 20:883–904. [https://doi.org/10.1016/S0191-8141\(98\)00020-0](https://doi.org/10.1016/S0191-8141(98)00020-0)
- Kohn MJ (2017) Titanite petrochronology. *Rev Mineral Geochem* 83:419–441. <https://doi.org/10.2138/rmg.2017.83.13>
- Kohn MJ, Corrie SL (2011) Preserved Zr-temperatures and U–Pb ages in high-grade metamorphic titanite: evidence for a static hot channel in the Himalayan orogen. *Earth Planet Sci Lett* 311:136–143. <https://doi.org/10.1016/j.epsl.2011.09.008>
- Kovaleva E, Klötzli U, Habler G et al (2017) The effect of crystal-plastic deformation on isotope and trace element distribution in zircon: combined BSE, CL, EBSD, FEG-EMPA and NanoSIMS study. *Chem Geol* 450:183–198. <https://doi.org/10.1016/j.chemgeo.2016.12.030>
- Kramers J, Frei R, Newville M et al (2009) On the valency state of radiogenic lead in zircon and its consequences. *Chem Geol* 261:4–11. <https://doi.org/10.1016/j.chemgeo.2008.09.010>
- Kunz BE, Regis D, Engi M (2018) Zircon ages in granulite facies rocks: decoupling from geochemistry above 850 °C? *Contrib Mineral Petrol* 173:1–21. <https://doi.org/10.1007/s00410-018-1454-5>
- Kusiak MA, Whitehouse MJ, Wilde SA et al (2013) Mobilization of radiogenic Pb in zircon revealed by ion imaging: implications for early Earth geochronology. *Geology* 41:291–294. <https://doi.org/10.1130/G333920.1>
- Kylander-Clark ARC (2017) Laser-ablation inductively coupled plasma. *Rev Mineral Geochem* 83:183–196
- Kylander-Clark ARC, Hacker BR, Cottle JM (2013) Laser-ablation split-stream ICP petrochronology. *Chem Geol* 345:99–112. <https://doi.org/10.1016/j.chemgeo.2013.02.019>
- Langone A, Padrón-Navarta José A, Ji WQ et al (2017) Ductile–brittle deformation effects on crystal-chemistry and U–Pb ages of magmatic and metasomatic zircons from a dyke of the Finero Mafic Complex (Ivrea–Verbano Zone, Italian Alps). *Lithos* 284–285:493–511. <https://doi.org/10.1016/j.lithos.2017.04.020>
- Larche FC, Cahn JW (1985) The interactions of composition and stress in crystalline solids. *Acta Metall* 33:331–357
- LaTourrette T, Wasserburg GJ, Fahey AJ (1996) Self diffusion of Mg, Ca, Ba, Nd, Yb, Ti, Zr, and U in haplobasaltic melt. *Geochim Cosmochim Acta* 60:1329–1340
- Lippmann F (1980) Phase diagrams depicting aqueous solubility of binary mineral systems. *N Jb Miner Abh* 139:1–25
- Liu Y, Hu Z, Gao S et al (2008) In situ analysis of major and trace elements of anhydrous minerals by LA-ICP-MS without applying an internal standard. *Chem Geol* 257:34–43. <https://doi.org/10.1016/j.chemgeo.2008.08.004>
- Love GR (1964) Dislocation pipe diffusion. *Acta Metall* 12:731–737
- Lucassen F, Franz G, Dulski P et al (2011) Element and Sr isotope signatures of titanite as indicator of variable fluid composition in hydrated eclogite. *Lithos* 121:12–24. <https://doi.org/10.1016/j.lithos.2010.09.018>
- Macdonald JM, Wheeler J, Harley SL (2013) Lattice distortion in a zircon population and its effects on trace element mobility and U–Th–Pb isotope systematics: examples from the Lewisian Gneiss Complex, northwest Scotland. *Contrib Mineral Petrol* 166:21–41. <https://doi.org/10.1007/s00410-013-0863-8>
- Marsh JH, Smye AJ (2017) U–Pb systematics and trace element characteristics in titanite from a high-pressure mafic granulite. *Chem Geol* 466:403–416. <https://doi.org/10.1016/j.chemgeo.2017.06.029>
- McClelland WC, Gehrels GE, Samson SD, Patchett PJ (1992) Structural and geochronologic relations along the western flank of the coast mountains batholith: Stikine River to Cape Fanshaw, central southeastern Alaska. *J Struct Geol* 14:475–489. [https://doi.org/10.1016/0191-8141\(92\)90107-8](https://doi.org/10.1016/0191-8141(92)90107-8)
- McDonough WF, Sun S-s (1995) The composition of the Earth. *Chem Geol* 120:223–253. [https://doi.org/10.1016/0009-2541\(94\)00140-4](https://doi.org/10.1016/0009-2541(94)00140-4)
- Migdisov AA, Williams-jones AE, Wagner T (2009) An experimental study of the solubility and speciation of the rare earth elements (III) in fluoride- and chloride-bearing aqueous solutions at temperatures up to 300 °C. *Geochim Cosmochim Acta* 73:7087–7109. <https://doi.org/10.1016/j.gca.2009.08.023>
- Migdisov AA, Williams-jones AE, Van HV, Salvi S (2011) An experimental study of the solubility of baddeleyite (ZrO₂) in fluoride-bearing solutions at elevated temperature. *Geochim Cosmochim Acta* 75:7426–7434. <https://doi.org/10.1016/j.gca.2011.09.043>
- Moore J, Beinlich A, Berndt J et al (2020) Microstructurally controlled trace element (Zr, U–Pb) concentrations in metamorphic rutile: an example from the amphibolites of the Bergen Arcs. *J Metamorph Geol* 38:103–127. <https://doi.org/10.1111/jmg.12514>
- Morozov IB, Smithson SB, Hollister LS, Diebold JB (1998) Wide-angle seismic imaging across accreted terranes, southeastern Alaska and western British Columbia. *Tectonophysics* 299:281–296. [https://doi.org/10.1016/S0040-1951\(98\)00208-X](https://doi.org/10.1016/S0040-1951(98)00208-X)
- Moser DE, Davis WJ, Reddy SM et al (2009) Zircon U–Pb strain chronometry reveals deep impact-triggered flow. *Earth Planet Sci Lett* 277:73–79. <https://doi.org/10.1016/j.epsl.2008.09.036>
- Ollierook HKH, Taylor RJM, Erickson TM et al (2019) Unravelling complex geologic histories using U–Pb and trace element systematics of titanite. *Chem Geol* 504:105–122. <https://doi.org/10.1016/j.chemgeo.2018.11.004>
- Pan Y, Fleet ME (1996) Rare earth element mobility during prograde granulite facies metamorphism: significance of fluorine. *Contrib Mineral Petrol* 123:251–262
- Papapavlou K, Darling JR, Storey CD et al (2017) Dating shear zones with plastically deformed titanite: new insights into the orogenic evolution of the Sudbury impact structure (Ontario, Canada). *Precambrian Res* 291:220–235. <https://doi.org/10.1016/j.precamres.2017.01.007>
- Papapavlou K, Darling JR, Moser DE et al (2018) U–Pb isotopic dating of titanite microstructures: potential implications for the chronology and identification of large impact structures. *Contrib Mineral Petrol* 173:82. <https://doi.org/10.1007/s00410-018-1511-0>
- Paterson B, Stephens WE, Herd DA (1989) Zoning in granitoid accessory minerals as revealed by backscattered electron imagery.

- Mineral Mag 53:55–61. <https://doi.org/10.1180/minmag.1989.053.369.05>
- Paton C (2011) Iolite: Freeware for the visualization and procession of mass spectrometric data. *J Anal at Spectrom* 26:2508–2518
- Paul AN, Spikings RA, Chew D, Daly JS (2019) The effect of intracrystal uranium zonation on apatite U–Pb thermochronology: a combined ID-TIMS and LA-MC-ICP-MS study. *Geochim Cosmochim Acta* 251:15–35. <https://doi.org/10.1016/j.gca.2019.02.013>
- Pearce NJG, Perkins WT, Westgate JA et al (1997) A compilation of new and published major and trace element data for NIST SRM 610 and NIST SRM 612 glass reference materials. *J Geostand Geoanal* 21:1–5. <https://doi.org/10.1111/j.1751-908X.1997.tb00538.x>
- Peterman EM, Reddy SM, Saxey DW et al (2016) Nanogeochronology of discordant zircon measured by atom probe microscopy of Pb-enriched dislocation loops. *Sci Adv* 2:e1601318. <https://doi.org/10.1126/sciadv.1601318>
- Piazolo S, La Fontaine A, Trimby P et al (2016) Deformation-induced trace element redistribution in zircon revealed using atom probe tomography. *Nat Commun* 7:1–7. <https://doi.org/10.1038/ncomms10490>
- Pouchon MA, Curti E, Degueldre C, Tobler L (2001) The influence of carbonate complexes on the solubility of zirconia: new experimental data. *Prog Nucl Energy* 38:443–446
- Putnis A (2009) Mineral replacement reactions. *Rev Mineral Geochem* 70:87–124. <https://doi.org/10.2138/rmg.2009.70.3>
- Putnis CV, Mezger K (2004) A mechanism of mineral replacement: isotope tracing in the model system KCl–KBr–H₂O. *Geochim Cosmochim Acta* 68:2839–2848. <https://doi.org/10.1016/j.gca.2003.12.009>
- Putnis CV, Tsukamoto K, Nishimura Y (2005) Direct observations of pseudomorphism: compositional and textural evolution at a fluid–solid interface. *Am Mineral* 90:1909–1912. <https://doi.org/10.2138/am.2005.1990>
- Rabier J, Puls MP (1989) Atomistic calculations of point-defect interaction and migration energies in the core of an edge dislocation in NaCl. *Philos Mag* 59:533–546. <https://doi.org/10.1080/01418618908229783>
- Rapp JF, Klemme S, Butler IB, Harley SL (2010) Extremely high solubility of rutile in chloride and fluoride-bearing metamorphic fluids: an experimental investigation. *Geology* 38:323–326. <https://doi.org/10.1130/G30753.1>
- Reddy SM, Timms NE, Trimby P et al (2006) Crystal–plastic deformation of zircon: a defect in the assumption of chemical robustness. *Geology* 34:257–260. <https://doi.org/10.1130/G22110.1>
- Rizvanova NG, Levchenkov OA, Belous AE et al (2000) Zircon reaction and stability of the U–Pb isotope system during interaction with carbonate fluid: experimental hydrothermal study. *Contrib Mineral Petrol* 139:101–114
- Romer RL, Heinrich ÆW, Schroder-Smeibidl et al (2005) Elemental dispersion and stable isotope fractionation during reactive fluid–flow and fluid immiscibility in the Bufa del Diente aureole, NE-Mexico: evidence from radiographies and Li, B, Sr, Nd, and Pb isotope systematics. *Contrib Mineral Petrol*. <https://doi.org/10.1007/s00410-005-0656-9>
- Rubatto D, Hermann J (2001) Exhumation as fast as subduction? *Geology* 29:3–6. [https://doi.org/10.1130/0091-7613\(2001\)029%3c0003:EAFAS%3e2.0.CO;2](https://doi.org/10.1130/0091-7613(2001)029%3c0003:EAFAS%3e2.0.CO;2)
- Ruiz-Agudo E, Putnis CV (2012) Direct observations of mineral–fluid reactions using atomic force microscopy: the specific example of calcite. *Mineral Mag* 76:227–253. <https://doi.org/10.1180/minmag.2012.076.1.227>
- Ruoff AL, Balluffi RW (1963) Strain-enhanced diffusion in metals. II. Dislocation and grain-boundary short-circuiting models. *J Appl Phys* 34:1848–1853
- Rusmore ME, Woodsworth GJ (1994) Evolution of the eastern Waddington thrust belt and its relation to the mid-Cretaceous Coast Mountains arc, western British Columbia. *Tectonics* 13:1052–1067. <https://doi.org/10.1029/94TC01316>
- Rusmore ME, Gehrels G, Woodsworth GJ (2001) Southern continuation of the Coast shear zone and Paleocene strain partitioning in British Columbia–Southeast Alaska. *Bull Geol Soc Am* 113:961–975. [https://doi.org/10.1130/0016-7606\(2001\)113%3c0961:SCOTCS%3e2.0.CO;2](https://doi.org/10.1130/0016-7606(2001)113%3c0961:SCOTCS%3e2.0.CO;2)
- Rusmore ME, Woodsworth GJ, Gehrels GE (2005) Two-stage exhumation of midcrustal arc rocks, Coast Mountains, British Columbia. *Tectonics* 24:1–25. <https://doi.org/10.1029/2004TC001750>
- Salvi S, Fontan F, Monchoux P et al (2000) Hydrothermal mobilization of high field strength elements in alkaline igneous systems: evidence from the Tamazeght Complex (Morocco). *Econ Geol* 95:559–576
- Schmitz MD, Bowring SA (2001) U–Pb zircon and titanite systematics of the Fish Canyon Tuff: an assessment of high-precision U–Pb geochronology and its application to young volcanic rocks. *Geochim Cosmochim Acta* 65:2571–2587. [https://doi.org/10.1016/S0016-7037\(01\)00616-0](https://doi.org/10.1016/S0016-7037(01)00616-0)
- Seydoux-Guillaume A-M, Montel J, Bingen B et al (2012) Low-temperature alteration of monazite: fluid mediated coupled dissolution–precipitation, irradiation damage, and disturbance of the U–Pb and Th–Pb chronometers. *Chem Geol* 330–331:140–158. <https://doi.org/10.1016/j.chemgeo.2012.07.031>
- Shannon RD (1976) Revised effective ionic radii and systematic studies of interatomic distances in halides and chalcogenides. *Acta Crystallogr* 32:751–767. <https://doi.org/10.1107/S0567739476001551>
- Smith MP, Storey CD, Jeffries TE, Ryan C (2009) In situ U–Pb and trace element analysis of accessory minerals in the Kiruna District, Norrbotten, Sweden: new constraints on the timing and origin of mineralization. *J Petrol* 50:2063–2094. <https://doi.org/10.1093/petrology/egp069>
- Smye AJ, Marsh JH, Vermeesch P et al (2018) Applications and limitations of U–Pb thermochronology to middle and lower crustal thermal histories. *Chem Geol* 494:1–18. <https://doi.org/10.1016/j.chemgeo.2018.07.003>
- Soman A, Geisler T, Tomaschek F et al (2010) Alteration of crystalline zircon solid solutions: a case study on zircon from an alkaline pegmatite from Zomba–Malosa, Malawi. *Contrib Mineral Petrol* 160:909–930. <https://doi.org/10.1007/s00410-010-0514-2>
- Spandler C, Hammerli J, Sha P et al (2016) MKED1: a new titanite standard for in situ analysis of Sm–Nd isotopes and U–Pb geochronology. *Chem Geol* 425:110–126. <https://doi.org/10.1016/j.chemgeo.2016.01.002>
- Spencer KJ, Hacker BR, Kylander-Clark ARC et al (2013) Campaign-style titanite U–Pb dating by laser-ablation ICP: implications for crustal flow, phase transformations and titanite closure. *Chem Geol* 341:84–101. <https://doi.org/10.1016/j.chemgeo.2012.11.012>
- Stacey JS, Kramers JD (1975) Approximation of terrestrial lead isotope evolution by a two-stage model. *Earth Planet Sci Lett* 26:207–221. [https://doi.org/10.1016/0012-821X\(75\)90088-6](https://doi.org/10.1016/0012-821X(75)90088-6)
- Stearns MA, Cottle JM, Hacker BR (2016) Extracting thermal histories from the near-rim zoning in titanite using coupled U–Pb and trace-element depth profiles by single-shot laser-ablation split stream (SS-LASS) ICP-MS. *Chem Geol* 422:13–24. <https://doi.org/10.1016/j.chemgeo.2015.12.011>
- Swiatnicki WA, Lojkowski W, Grabski MW (1986) Investigation of grain boundary diffusion in polycrystals by means of extrinsic grain boundary dislocations spreading rate. *Acta Metall* 34:599–605
- Syverson DD, Etschmann B, Liu W et al (2019) Oxidation state and coordination environment of Pb in U-bearing minerals. *Geochim*

- Cosmochim Acta 265:109–131. <https://doi.org/10.1016/j.gca.2019.08.039>
- Thomas JB, Sinha AK (1999) Field, geochemical, and isotopic evidence for magma mixing and assimilation and fractional crystallization processes in the Quottoon Igneous Complex, northwestern British Columbia and southeastern Alaska. *Can J Earth Sci* 36:819–831. <https://doi.org/10.1139/e99-001>
- Timms NE, Kinny PD, Reddy SM (2006) Enhanced diffusion of Uranium and Thorium linked to crystal plasticity in zircon. *Geochem Trans* 7:1–16. <https://doi.org/10.1186/1467-4866-7-10>
- Timms N, Kinny P, Reddy SM et al (2011) Relationship among titanium, rare earth elements, U–Pb ages and deformation microstructures in zircon: implications for Ti-in-zircon thermometry. *Chem Geol* 280:33–46
- Tomaschek F, Kennedy AK, Villa IM et al (2003) Zircons from Syros, Cyclades, Greece—recrystallization and mobilization of zircon during high-pressure metamorphism. *J Petrol* 44:1977–2002. <https://doi.org/10.1093/petrology/egg067>
- Tullis J, Yund RA (1987) Transition from cataclastic flow to dislocation creep of feldspar: mechanisms and microstructures. *Geology* 15:606–609
- Turnbull D, Hoffman R (1954) The effect of relative crystal and boundary orientations on grain boundary diffusion rates. *Acta Metall* 2:419–426
- Vard E, Williams-jones AE (1993) A fluid inclusion study of vug minerals in dawsonite-altered phonolite sills, Montreal, Quebec: implications for HFSE mobility. *Contrib Mineral Petrol* 113:410–423
- Walters JB, Kohn MJ (2017) Protracted thrusting followed by late rapid cooling of the Greater Himalayan Sequence, Annapurna Himalaya, Central Nepal: Insights from titanite petrochronology. *J Metamorph Geol* 35:897–917. <https://doi.org/10.1111/jmg.12260>
- Watson EB, Liang Y (1995) A simple model for sector zoning in slowly grown crystals: implications for growth rate and lattice diffusion, with emphasis on accessory minerals in crustal rocks. *Am Mineral* 80:1179–1187. <https://doi.org/10.2138/am-1995-11-1209>
- Weinberg RF, Wolfram LC, Nebel O et al (2020) ScienceDirect Decoupled U–Pb date and chemical zonation of monazite in migmatites: the case for disturbance of isotopic systematics by coupled dissolution-reprecipitation. *Geochim Cosmochim Acta* 269:398–412. <https://doi.org/10.1016/j.gca.2019.10.024>
- Williams IS (1998) U–Th–Pb geochronology by ion microprobe. *Rev Econ Geol* 7:1–35
- Williams ML, Jercinovic MJ, Harlov DE et al (2011) Resetting monazite ages during fluid-related alteration. *Chem Geol* 283:218–225. <https://doi.org/10.1016/j.chemgeo.2011.01.019>
- Wood DJ, Stowell HH, Onstott TC, Hollister LS (1991) $^{40}\text{Ar}/^{39}\text{Ar}$ constraints on the emplacement, uplift, and cooling of the Coast Plutonic Complex sill, southeastern Alaska. *Geol Soc Am Bull* 103:849–860

Publisher's Note Springer Nature remains neutral with regard to jurisdictional claims in published maps and institutional affiliations.